lajss.org
Latin American Journal of Solids and Structures
www.lajss.org

# Numerical and Experimental Investigation of Surface Explosion Induced Crater Formation Using a Coupled Eulerian Lagrangian Approach

**Dursun BAKIR 1[a]* ORCID**

[a] Civil Engineering, Faculty of Engineering and Architecture, Bitlis Eren University, Bitlis, Turkey1. Email:dbakir@beu.edu.tr

* Corresponding author

## Abstract

Ground contact explosions do not cause significant deformation or crater formation on the ground. This situation is of critical importance in forensic explosion analysis and blast-resistant structural design. In this study, a multiscale numerical model based on the Coupled Eulerian–Lagrangian (CEL) method was developed in Abaqus/Explicit software to model craters formed as a result of contact explosions applied to the ground. The model was calibrated using controlled field tests conducted on low-plasticity clay-silt (CL) soil with 1, 2, and 3 kg of TNT equivalent and validated using a real vehicle-induced explosion event that occurred in Elazığ in 2016 with approximately 2 tons of TNT equivalent on soil with the same properties. Soil behavior was defined using the Mohr–Coulomb plasticity model, while explosive behavior was defined using the Jones–Wilkins–Lee (JWL) state equation. Basic geometric parameters such as crater diameter, depth, depth/diameter ratio, and blast index were evaluated across three orders of explosive mass. The numerical results were found to be consistent with field measurements; error rates were below 5% for small-scale experiments and below 8% for large-scale explosions. The results show that as the explosive mass increases, craters become proportionally wider and deeper due to increased lateral energy dispersion. The developed CEL-based numerical approach provides a reliable engineering tool for forensic explosion analysis and the evaluation of ground behavior under extreme loading.

## Keywords

Forensic blast analysis, surface contact explosion, crater formation, coupled Eulerian–Lagrangian (CEL), explosion reconstruction, blast–soil interaction, geotechnical response

## Graphical Abstract

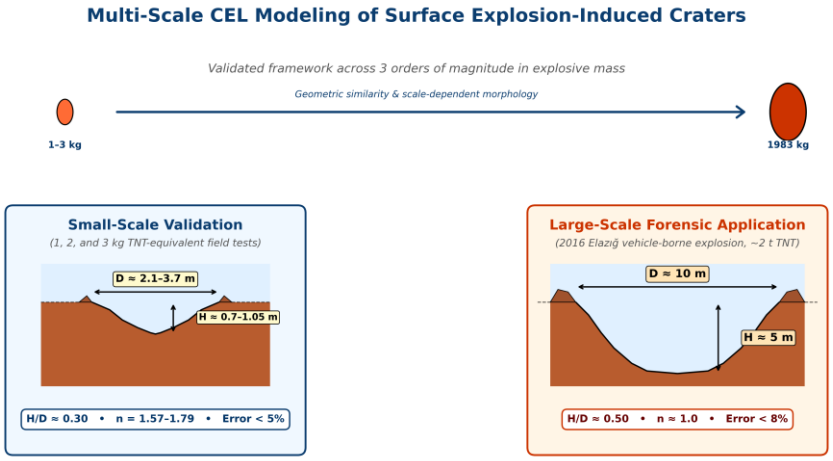

## 1 INTRODUCTION

Explosions from man-made explosives result in ground cratering (Waga & Fajer, 2021). The size of the explosion determines how big and deep the craters are(Ambrosini et al., 2002; M. Wang et al., 2018; W. Wang et al., 2015); these factors are critically important for the success of post-disaster rescue operations(Fang et al., 2020) and for studying and measuring the effects of explosions(Dolejš et al., 2020). When an explosion hits the ground, it turns into mechanical and thermal energy, which causes the ground to deform and form craters(I.-T. Wang, 2019). The shock wave from the explosion pushes down on the ground, and the impulse effect on the ground makes a crater. The size of the crater is affected by how powerful the shock wave is and what kind of material the wave travels through(Jayasinghe et al., 2014). In this context, the 2016 car bomb attack on the security unit in Elazığ province, Turkey, was studied, along with the size of the crater left on the ground after the explosion and the damage done to the buildings around the explosion site. A forensic approach was used to figure out how much explosive was used and to check the damage that was done(Savaş & Bakir, 2023). Finding the blast point, the type of explosive used, and the amount of explosive mass are all part of the forensic approach(van der Voort et al., 2015). Looking into how the ground crater formed after the blast helps figure out how to plan blasting operations. Field experiments and theoretical analyses are employed to ascertain and enhance blasting design parameters(Wu et al., 2025). Equation 1 graphically shows a quasi-empirical way to figure out blast wave parameters based on scaled distance(Hussein & Heyliger, 2025a) .

$$Z = \frac{R}{W^{\frac{1}{3}}} \tag{1}$$

Z is the scaled distance, R is the distance (m) between the explosive and the point of interest, and W is the weight of the explosive (kg, TNT equivalent). The equation's scaled distance (Z) shows that the distance between the explosive and the structure is inversely proportional to the cube root of the amount of explosive. Utilizing this scaled distance, positive phase parameters contingent on the Z value are established for hemispherical TNT explosions at sea level, in accordance with the Unified Facility Criteria (UFC)(Defense, 2008) (Figure 1). When explosions happen on the ground, the energy release is hemispherical, which means that, unlike explosions in free air, pressure levels and positive phase durations can be higher. The UFC's rules for hemispherical TNT explosions are often used for explosions that happen on the ground. They are very important, especially when it comes to scaling and analyzing big explosions in both real-life and computer-based studies. The explosion at the port of Beirut on August 4, 2020, affected a significant amount of Beirut and countries that are more than 250 kilometers away, like Turkey, Syria, Israel, and Cyprus. Where the explosion happens will determine the shape and size of the crater. The crater that was made is about 120 m wide and 4.5–5 m deep. It is said that the depth would be greater if there were no water in the area(Sadek S. et al., 2021).

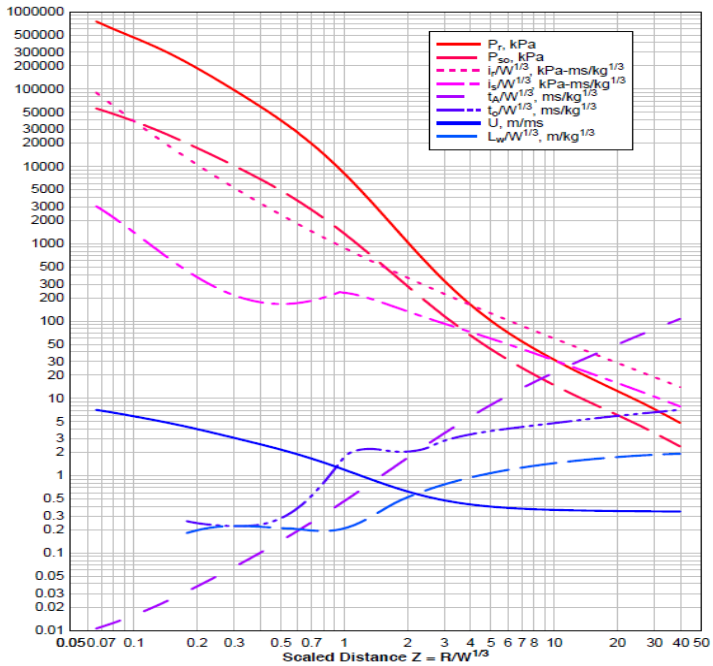


**Figure 1** Logarithmic graph of free air blast with scaling factor

In 2016, a truck full of about 2 tons of explosives was used in a suicide attack in Elazığ, Turkey. The truck hit the ground and exploded, making a crater that was about 10 m wide and 5 m deep. The size of the craters left behind by these huge explosions is very important for forensic and engineering purposes because they can help figure out how much explosive was used and where it went off. The creation of blast-induced craters is controlled by a complicated interaction between the air around them, the properties of the soil, and the physical and mechanical properties of the explosive material. Prior experimental and analytical investigations have established a significant correlation between crater geometry, specifically diameter and depth, and the explosive charge in ground-contact and surface detonations. Experimental studies and numerical analyses have demonstrated that crater dimensions can be employed to validate soil constitutive models and numerical solution methodologies when juxtaposed with field measurements(Ambrosini & Luccioni, 2006). Rongzheng Xu et al. conducted extensive field experiments utilizing 1, 3, and 10 tons of TNT in direct contact with the ground to investigate crater morphology, including shape, depth, and diameter. They proposed analytical models for predicting crater diameters in contact explosion scenarios (Xu et al., 2021). In the same way, empirical formulas have been made to figure out the diameter, depth, and volume of craters based on the amount of TNT used for surface explosions in different types of soil. This shows how much crater shape depends on the weight of the explosive and the type of soil(Adushkin & Khristoforov, 2004). Further research has explored crater formation mechanisms by positioning explosives perpendicularly to the ground surface and analyzing the resultant ground deformation and failure patterns(I.-T. Wang, 2021) . Even with these efforts, there are still not many numerical studies on surface and ground-contact explosions, especially for large explosive charges(Keskin et al., 2022; Mobaraki & Vaghefi, 2015; Stevens & Krauthammer, 1991). Later studies used the ALE method to look into how soil near the surface reacts and how underground structures respond to surface blast loading(N. Nagy, 2025). Haimin Qian et al. investigated the blast resilience of service tunnels subjected to vehicle-borne contact explosions, emphasizing safe burial depth and tunnel wall thickness through ALE-based numerical models(Qian et al., 2021). The Coupled Eulerian–Lagrangian (CEL) method is a well-known numerical tool for modeling large deformations and complicated interactions between soil, explosives, and structures when there is a lot of stress(Benson, 1992; Chen et al., 2019; Hussein & Heyliger, 2025b; C. Liu et al., 2025; Maier et al., 2025; G. Yang et al., 2018). Nonetheless, a significant deficiency persists in the literature: although the CEL methodology has been extensively utilized for blast-structure interaction issues, its application in simulating blast-induced crater formation resulting from large-scale ground-contact explosions remains notably constrained. More importantly, no previous study has numerically modeled a real large-scale explosive attack using the CEL method and systematically validated the model through controlled small-scale explosion experiments conducted under identical soil conditions. To fill this gap, this study creates a CEL-based numerical modeling framework in ABAQUS/Explicit to simulate the creation of craters caused by a real-world vehicle-borne explosive attack with about 2 tons of explosives. The numerical findings were supported by forensic evidence obtained from the 2016 Elazığ vehicle-borne explosive incident(Savaş & Bakir, 2023) as well as by a series of controlled field experiments performed at the same site using TNT-equivalent charges of 1, 2, and 3 kg under identical soil conditions. This study addresses a significant gap in the existing literature by using the Coupled Eulerian–Lagrangian (CEL) method to numerically validate the formation of explosion-induced craters for explosions of different magnitudes. The literature has generally progressed in the realm of numerical modeling and has not included a direct correlation with actual large-scale explosion events through a small number of experimental measurements. In contrast, this study simulates a real explosive attack and validates it through controlled small-scale field experiments conducted under the same ground conditions. We also suggest an improved numerical discretization scheme that finds a balance between speed and accuracy in predictions.This feature enhances the practical value of the CEL-based framework for forensic blast assessment, explosive charge estimation, and the engineering design of structures subjected to extreme blast loading. The present study builds upon and substantially extends a preliminary investigation by the author (Bakır, 2025), where the CEL method was demonstrated for a single 3 kg TNT ground-contact explosion as a methodological proof-of-concept. The present work extends this in five major directions: (1) systematic small-scale validation with nine field tests (1, 2, and 3 kg); (2) extension to a 1983 kg vehicle-borne event (the 2016 Elazığ attack), reconstructed forensically for the first time using CEL; (3) two-tier Eulerian domain scaling with independent mesh-sensitivity analyses; (4) scale-dependent crater morphology analysis through the blast index n and H/D ratio; and (5) independent TNT-equivalence calibration for the specific TNG batch used in this campaign. Together, these extensions transform a single-case methodological demonstration into a validated, multi-scale, forensic-engineering framework.

## 2 Test site and calculation of the TNT equivalent

The field tests took place in Elazığ, Turkey, about 3 km from where the attack happened in 2016 (Savaş & Bakir, 2023). The soil used for the tests had the same geotechnical properties as the soil at the attack site. Standard Penetration Tests (SPT) produced blow counts between N = 6 and 12 blows per 30 cm, and additional laboratory analyses categorized the soil as low-plasticity clayey silt (CL). The unit weight of the soil was $\gamma = 12.5–14.3$ kN/m³, the water content was w = 9.6–19.3%, the cohesion was c = 100 kPa, and the internal friction angle was $\phi = 24°$ (Table 1)(Keskin et al., 2022). The phreatic level was not found within the 5 m drilling depth, which showed that the subsurface was very dry. The soil profile had brown clayey silt with organic matter from 0 to 0.7 m, and reddish-brown clayey silt from 0 to 5 m. The Mohr-Coulomb constitutive model used for the numerical simulations used these geotechnical parameters. There were controlled field explosions with explosive charges of 1 kg, 2 kg, and 3 kg, spaced 5 m apart. The 1 kg charge had an explosive volume of 0.3146 m³, the 2 kg charge had an explosive volume of 0.4449 m³, and the 3 kg charge had an explosive volume of 0.5448 m³. Trinitroglycerin (TNG) used in this study was supplied by Orica Nitro, and its relevant material properties are summarized in Table 2(*Orica-Nitro Explosives*, 2023). To allow meaningful comparison between different energetic materials, the TNT equivalence method well established in the literature is commonly employed. Thus, the blast effect was evaluated as the TNT equivalent of the TNG explosive used in the experiment. Thus, the blast effect was evaluated as the TNT equivalent of the TNG explosive used in the experiment(Criteria(UFC), 2008; Edri et al., 2019; Esparza, 1986; Formby & Wharton, 1996; PW., 1996; Wharton et al., 2000). For this reason, when performing the blast analysis, the parameters of the TNT explosive were used in proportion to the equivalence calculation of the TNG used in the experiment. For this reason, the effect of the TNG explosive charge is calculated and used relative to the effects of TNT explosives. Therefore, the TNT equivalence is determined by the ratio of the mass of TNG used in the experiment to the calculated equivalent TNT mass (Grisaro & Edri, 2017). The behavior of the explosion pressure is affected by the type and chemical composition of the explosive. Even if explosives have equal mass and geometry, they exhibit different explosion behaviors due to differences in density, energy release rate, and specific energy parameters (Cooper, 1994; King & Vaught, 2008). For this reason, the use of a standardized reference explosive is essential. Trinitrotoluene (TNT) is typically selected for this role owing to the abundance of experimental data and its long-standing acceptance in blast research(Sochet, 2010). TNT equivalency compares the amount of energy released by an explosive to the amount of TNT that would release the same amount of energy. This is how the TNT equivalence factor is defined. An equivalency test setup with a sensor-to-explosive distance of 3.2 m was used to find out how much TNT the TNG explosive used in this study was equivalent to. Table 3 shows the distance between the explosive and the ground, the height of the steel rods that hold the sensors, and the distance between the explosive and the pressure sensors. The equivalence values obtained align with those documented for analogous explosives in the literature(Savaş & Bakir, 2022; Zhou et al., 2008). Figure 2 shows that the sensors recorded histories of positive and negative pressure over time, following the scaled distance definition in Equation 1, Z (m/kg$^{1/3}$). We used scaled-distance-based methods to figure out the pressures acting on the plate surface because of the explosion. We assumed that the TNG explosive had a TNT value of 0.91.The tests showed both positive and negative pressure phases. Based on the measured peak positive pressure, the UFC graph in Figure 1 was used to find the scaled distance (Z) that matched the ambient pressure ($P_{so}$). Next, the explosive's TNT equivalent was figured out using the formula in Equation 1. We used a PCB piezoelectric pressure transducer pen (Figure 3) to get ambient pressure-time data. The pen was placed axially with respect to the explosion source and at an angle to the direction of the blast wave propagation. To keep the pressure pen in place, it was placed on the ground and raised with a steel rod (Figure 2). It was then held in place with removable fasteners.The data acquisition system had three PCB piezoelectric reflected pressure transducers, one PCB piezoelectric ambient pressure pen, a 16-channel Oros OR36 data logger that could record up to 51,200 data points per second per channel, and a laptop with NV Gate software (Figure 4)(*Oros-Or36-Datalogger*, 2023). After the test system was set up, ambient pressure measurements were taken to find out how much TNT the Orica-brand explosive was worth. The pressure data were taken over a period of 0.02 seconds. In the pressure–time history (Figure 5), the values beyond 0.010 s had the same four-digit decimal values. Because of this, these data points were left out of the pressure–time plot but kept in the impulse–time plot (Figure 6). The UFC ambient pressure curve (Figure 5) showed that the peak positive pressure of 52.924 N/m² (52.924 Pa) happened when the scaled distance (Z) was 3.87. For a distance of 3.20 m between the explosive and the sensor, Equation 1 gave an equivalent TNT weight ($W_{tnt}$) of 0.57 kg. In summary, as shown in Table 4, the TNG explosive is about 62% equivalent to TNT (Equation (2)). Using the scaled distance from the sensor measurements and the corresponding pressure values, we were able to

figure out the equivalent explosive weight ($W_{TNT}$ = 0.57 kg).

Here, the relative effectiveness factor according to TNG is in terms of TNT;

$$\frac{W_{TNG}}{W_{TNT}} = \frac{0.91}{0.57} = 0.62 \quad (2)$$

**Table 1** Soil test results

| Depth (m) | Phreatic Level | SPT tests | | HD | DD | w (%) | T200 | LL (%) | PI (%) | Class. USCS |
|---|---|---|---|---|---|---|---|---|---|---|
| | | **Depth (m)** | **N** | | | | | | | |
| 0.7 | Without phreatic water | 0.5–1.0 | 6 | 1.25 | 1.14 | 9.6 | 87 | 28.1 | 12.3 | CL |
| 1.0 | | 1.5–2.0 | 12 | 1.43 | 1.27 | 12.7 | 91 | 27.9 | 8.6 | CL |
| 2.0 | | | | | | | | | | |
| 3.0 | | | | | | 19.3 | 95 | 31.0 | 10.4 | CL |
| 4.0 | | | | | | | | | | |
| 5.0 | | | | | End of the drilling | | | | | |

**Soil Profile**

| **Depth, m** | **Soil type** |
|---|---|
| 0 to 0.7 | Brown clayey silt with organic matter |
| 0.7 to 5 | Reddish brown clay silt of low plasticity, classification CL, very dry. |

**Table 2** TNG properties (*Orica-Nitro Explosives*, 2023)

| Explosive Properties Used in the Experiment | |
|---|---|
| Ideal Detonation Velocity (m/s) | 6140 |
| Ideal Detonation Pressure (atm) | 112900 |
| Ideal Detonation Temperature (K) | 3106 |
| Density(gr/cm³) | 1.20 |
| Water Resistance | Great |
| Ideal Explosion Temperature (kJ / Kg.) | 4370 |
| Ideal Gas Volume (Lt / Kg) | 873 |
| Relative Effective Energy (%)in comparison to ANFO | 129 |
| Relative Bulk Strength (%)in comparison to ANFO | 193 |

**Table 3** Layout of the Experimental setup

| | |
|---|---|
| Stand-off Distance m | 1.855 |
| Explosive Weight (W kg) | 0.91 |
| Sensor Elevation(m) | 1.85 |
| Explosive-Sensor Distance (m) | 3.2 |


**Figure 2** Sensors and explosive placement

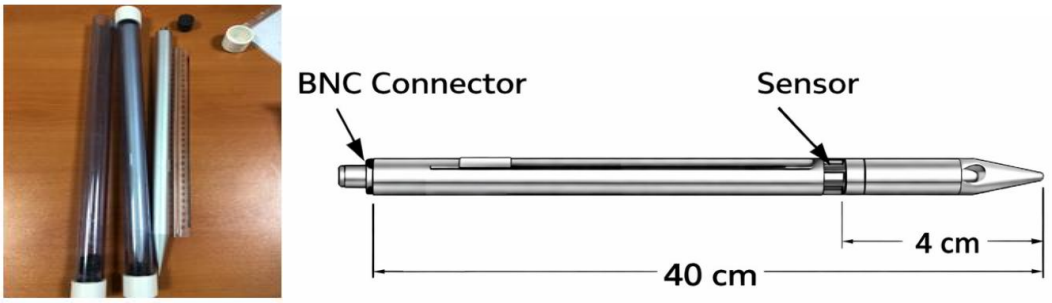


**Figure 3** PCB Piezoelectric Pressure Transducer Pen and Detail

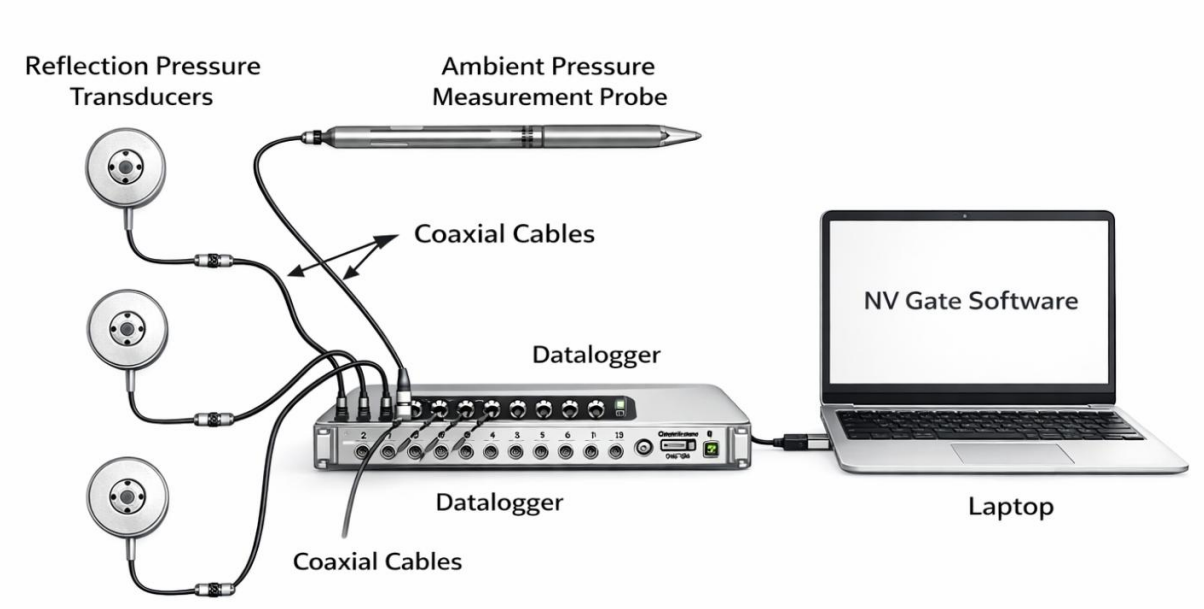


**Figure 4** Data Acquisition System

**Table 4** Calculated sensor values

| SENSOR | Max Pressure | | Min Pressure | | Z (m/kg1/3) | W (kg) |
|---|---|---|---|---|---|---|
| | Time | Pressure (N/m2) | Time | Pressure (N/m2) | | |
| | 8.590 | 52.924 | 8.5942 | -11795.8 | 3.8663 | 0.5702 |

The pressure–time history from the data acquisition system (Figure 5) shows the first shock from the ambient pressure wave and then the second shock from the pressure bouncing off the ground. Figure 6 shows the cumulative impulse–time curve that was made from the pressure–time data. This clearly shows the time-dependent nature of the blast loading. Even though the positive phase only lasted about 2 ms, it created a strong impulse of about 18 kPa·ms, which means that a sudden and strong pressure was put on the structure. The negative phase, on the other hand, lasted longer (about 20 ms) and made an impulse of about −14.5 kPa·ms. The net impulse stayed positive at about 3.5 kPa·ms, though, because the positive phase was stronger. The calculated data shows that the peak overpressure parameter is insufficient to evaluate the blast effect. The positive impulse is an important parameter for the damage caused by the explosion. The cumulative impulse is an important parameter for evaluating the destructive effect of the explosion. Indeed, a characteristic feature of surface explosions is that the positive phase duration ($t^+$ = 2 ms) is shorter than the negative phase duration ($t^-$ = 20 ms). In this case, the reflected effect from the ground increases the reflection peak pressure while also shortening the duration of the positive phase. The ratio of the positive impulse to the negative impulse ($I^+/I^-$ = 18/14.5 = 1.24) confirms that the positive impulse affected the total load. This result is confirmed when looking at the damage models observed after the 2016 Elazığ attack (Savaş & Bakir, 2023). Accordingly, this result supports the use of positive-phase blast parameters in the subsequent numerical analyses.

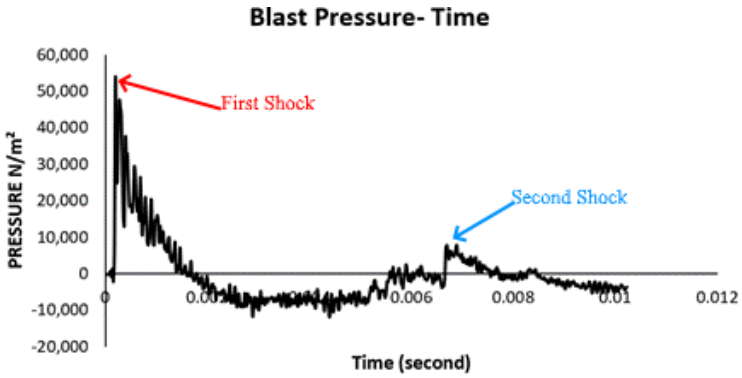


**Figure 5** Blast pressure-time graphic

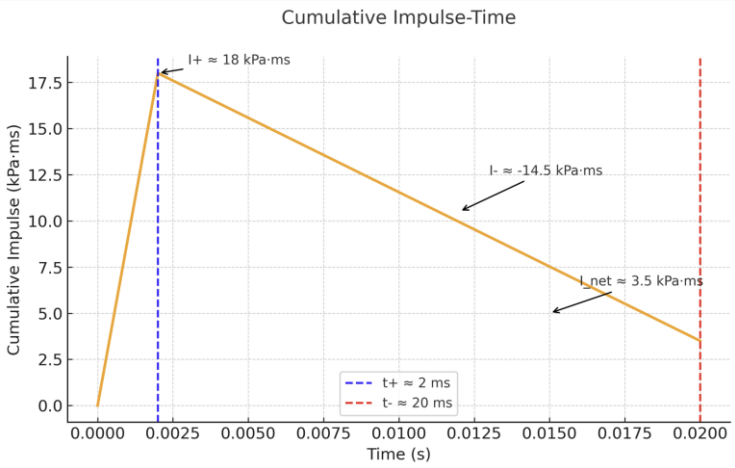


**Figure 6** Cumulative Impuls-time graphic

### 2.1 Crater Formation Tests (1-2-3 kg TNG)

This study encompasses a series of field-scale ground-contact explosion tests utilizing nine TNT-equivalent explosive charges. Three 1 kg, three 2 kg, and three 3 kg TNT-equivalent charges were set off directly on the ground. An electric detonator was used to set off each explosive. There were two parts to the experimental program. Three 1 kg explosive charges were set off at the same time in the first stage. The 2 kg and 3 kg charges were set off one after the other in the second stage. Figure 7 shows that the distance between all of the explosive charges was kept at a constant 5 m to avoid any effects that might happen when two charges go off next to each other. Figure 8 shows the craters that were made by the explosions.

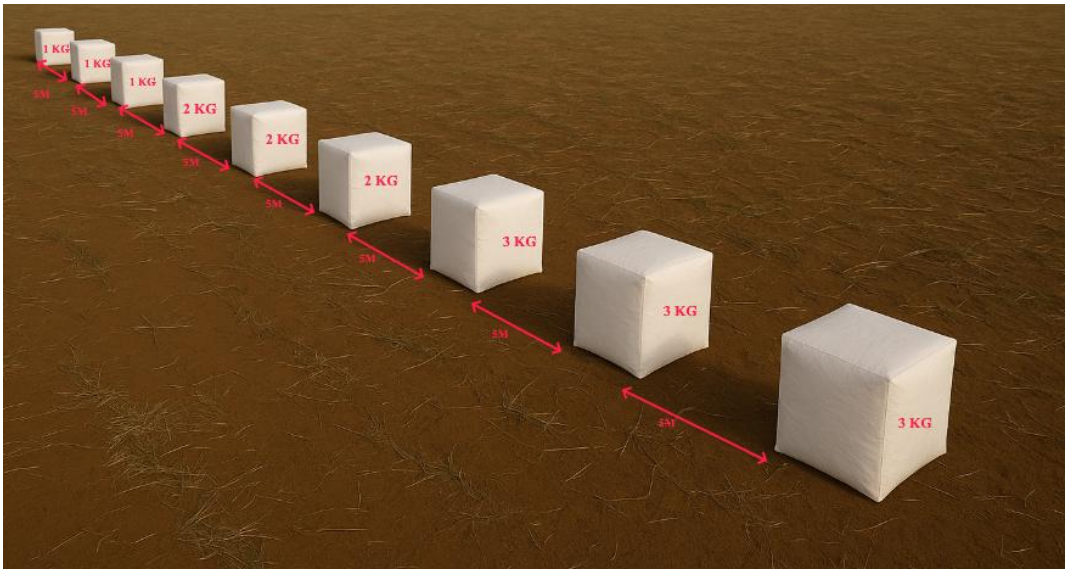


**Figure 7** Schematic placement of explosives in the field

The primary objective of these tests was to see how different charge weights of surface explosions affect the shape of craters and the ground response. The experimental data acquired from these tests were subsequently employed for the calibration and validation of numerical modeling studies. We measured the size of the craters using the definitions of crater size suggested by Ambrosini et al. (Figure 8)(Ambrosini et al., 2002). The main geometric factors taken into account were the crater diameter (D) and crater depth (H). For crater calculations, the diameters D and Df and the heights $H_1$ and $H_2$ were measured. Since there was a negligible difference between the heights $H_1$ and $H_2$, $H_1$ was accepted as the crater height. The complete set of crater dimensions obtained from the nine explosion tests is summarized in Table 5.To evaluate variations in crater geometry and the associated soil response, the blast action index (n) was calculated using Equation (3). This provides us a number that shows how much soil dispersion and ejection played a role in making the crater. It shows how the energy from the blast spreads out in the ground(Xu et al., 2021). Based on the experimental measurements, the calculated blast index values ranged from 1.57 to 1.79.

$$n = (\frac{D}{2})/H \tag{3}$$

Figure 9 shows an obvious correlation between the weight of the explosive charge and the size of the crater that forms. The more explosive material you use, the bigger both the diameter and depth of the crater become. The average diameter and depth of the craters from the tests with 1 kg of explosives were 2.09 m and 0.65 m, in that order. For the 2 kg charges, these numbers went up to 2.89 m and 0.85 m. When the maximum explosive charge was 3 kg, the crater diameter grew to 3.63 m and the crater depth grew to 1.05 m. There were also circumferential cracks around the crater that were between 0.03 and 0.04 m wide, as well as a clear uplifted zone with an average diameter of about 5 m. The experimental findings demonstrate that crater diameter increases logarithmically rather than linearly with the augmentation of explosive mass. The D/H ratios we measured, which range from 3.0 to 3.5, are in line with what Kinney and Graham(Kinney, G. F., Graham, 2013) found, which was that the depth of a crater is about one-fourth of its diameter, depending on the ground conditions. The computed blast index values (n = 1.57–1.79) are consistent with the typical range for shallow, broad craters resulting from surface explosions in cohesive soils. Ambrosini et al. (2002)claim that blast index values higher than n > 1.5 mean that a lot of the explosion energy is lost sideways instead of up and down. This is in line with the crater shapes seen in this study. The clayey soil at the test site is to blame for this behavior. It

makes it harder for things to go straight down but easier for things to move sideways. The crater that formed during the 2016 Elazığ attack had a blast index of n = 2.0 (Table 5), which means that the energy was spread out more evenly across the sides. This difference is probably due to the much larger amount of explosives used (2 tons instead of 1 to 3 kg) and the fact that the explosives were in a vehicle, which may have caused them to be contained.

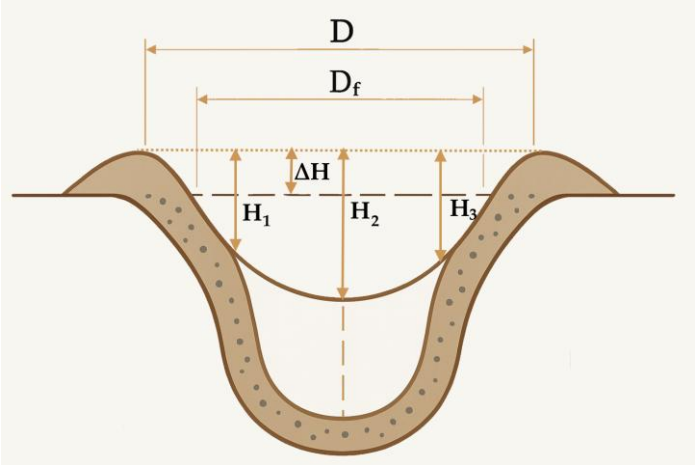


**Figure 8** Crater dimensions diagram

**Table 5** Crater measurements

| Test | $W_{TNG}$ (kg) | $W_{TNT}$ (kg) | D (m) | $D_f$ (m) | $D_{Ave.}$ (m) | $H_1$ (m) | $H_2$ (m) | $H_{Ave.}$ (m) | n |
|---|---|---|---|---|---|---|---|---|---|
| 1 | 1 | 1.612 | 2.15 | 2.05 | 2.10 | 0.60 | 0.70 | 0.65 | 1.62 |
| 2 | 1 | 1.612 | 2.20 | 2.05 | 2.13 | 0.65 | 0.70 | 0.68 | 1.57 |
| 3 | 1 | 1.612 | 2.05 | 2.00 | 2.03 | 0.60 | 0.65 | 0.63 | 1.61 |
| 4 | 2 | 3.23 | 2.95 | 2.85 | 2.90 | 0.80 | 0.90 | 0.85 | 1.71 |
| 5 | 2 | 3.23 | 3.00 | 2.90 | 2.95 | 0.85 | 0.90 | 0.88 | 1.67 |
| 6 | 2 | 3.23 | 2.85 | 2.80 | 2.83 | 0.80 | 0.85 | 0.83 | 1.70 |
| 7 | 3 | 4.84 | 3.70 | 3.50 | 3.60 | 1.00 | 1.10 | 1.05 | 1.71 |
| 8 | 3 | 4.84 | 3.65 | 3.55 | 3.60 | 1.05 | 1.10 | 1.08 | 1.67 |
| 9 | 3 | 4.84 | 3.80 | 3.60 | 3.70 | 1.00 | 1.05 | 1.03 | 1.79 |

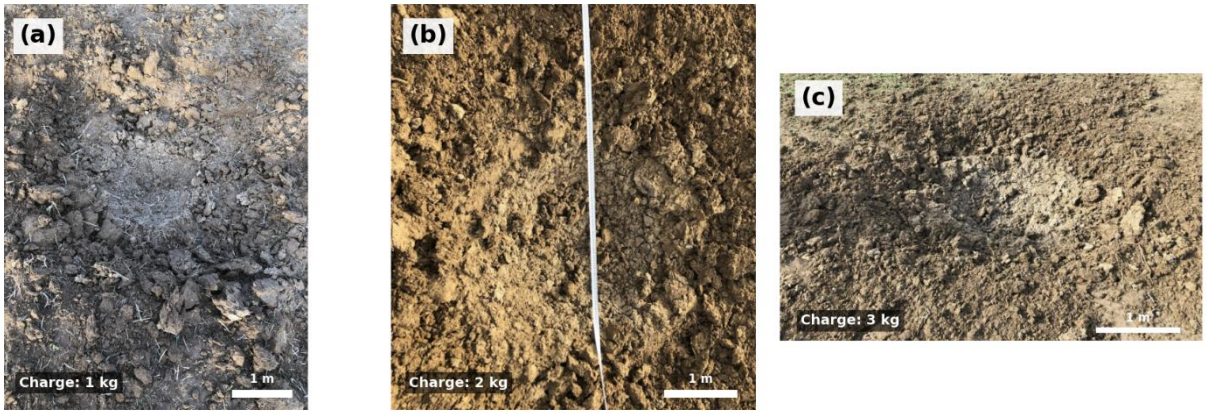


**Figure 9** Crater dimensions measured at the explosion site;
**a)**1 kg **b)**2kg **c)**3kg

### 2.2 Suicide attack in Elazig Province in Turkey in 2016

In 2016, a suicide assault in Elazığ province, Turkey, used a minibus containing around 2 tons of explosives, which detonated, resulting in a crater roughly 10 meters in diameter and 5 meters deep at the explosion location(Figure10). The blast index is 1, signifying that the crater's depth is roughly half of its diameter(Table 6). This indicates that the crater formed is not a deep crater but rather a comparatively shallow and broad crater. The literature indicates that the D/H ratio in extensive surface explosions typically ranges from 1.8 to 2.2(Kinney, G. F., Graham, 2013), and the numbers derived in this investigation align with the existing literature. Examination of the resulting crater indicates that the pressure generated by the explosion

caused significant surface deformation around the crater. Explosions occurring on the ground with an explosion index (n) of 1 are defined as wide and shallow craters (Kinney & Graham, 2013) .In this explosion (Fig. 10), the explosion index of 1, as measured in the crater geometry dimensions (Table 6), confirms the crater characteristics.

**Table6** Suicide attack crater measurements

| W (ton) | $D_{ort}$ (m) | $H_{ort}$ (m) | n |
|---|---|---|---|
| 1983 | 10 | 5 | 1 |


**Figure 10** Forensic field measurements of the crater geometry formed at the explosion site

## 3 CEL model

Surface explosion-induced crater formation is a complex, nonlinear, multi-phase dynamic process. As schematically illustrated in Figure 11, it can be conceptually divided into four sequential phases: (i) the detonation (chemical reaction) phase, during which the JWL-governed energy release initiates the explosion; (ii) the shock wave propagation phase, in which spherical shock fronts expand through both the air and the soil at different velocities; (iii) the gas expansion and crater excavation phase, where the high-pressure detonation gases push the soil outward and upward, forming the crater walls and ejecting material; and (iv) the ejecta fallback and final crater phase, during which the displaced soil settles back and the final crater geometry stabilizes. The Coupled Eulerian–Lagrangian (CEL) framework employed in this study is well suited to capture all four phases through its handling of large deformation flow, material interface tracking, and shock wave propagation in both the gas and the soil domains.

The Cel model optimizes the analysis of damage behavior, deformations, and resulting interactions by combining Eulerian and Lagrangian equations in cases involving complex loading such as explosions. It combines the two equations by optimizing them in the modeling of continuous fields(Benson, 1992; Souli & Shahrour, 2013; Veen, 2003; G. Yang et al., 2018). In the Lagrangian approach, the material and mesh deform together, and the stress at the material interfaces is clearly tracked. However, under conditions of large deformation caused by large loads, this approach causes significant mesh distortion, leading to numerical instability in the calculation. In the Cel method, the two approaches are optimized in a single algorithm, eliminating the problems that arise in the two separate approaches. While structural components are modeled using the Lagrangian approach, air, ground, and explosives are modeled using the Eulerian model as environments that can deform significantly(H. Yang et al., 2025). The CEL method algorithm operates in two stages. First, material deformation is calculated using the Lagrange formulation. Then, the Eulerian remapping step is applied to transfer the deformed material to a fixed Eulerian mesh. Interactions between Lagrangian and Eulerian domains are handled using general-purpose contact algorithms (Dolatshahi & Qarahasanlou, 2023; Qiu et al., 2009) , without requiring topological connectivity or shared nodes between the meshes. In this interaction scheme, Eulerian elements impose pressure boundary conditions on Lagrangian surfaces, while Lagrangian elements define displacement constraints for the Eulerian domain, enabling accurate representation of fluid–structure interfaces.Within the CEL framework, the detonation behavior of explosive materials is commonly described using the Jones–Wilkins–Lee (JWL) equation of state, while surrounding geological materials, such as soil, may be modeled using simplified elastic–plastic constitutive

formulations. This combination allows the CEL method to effectively capture shock wave propagation, large deformation patterns, and permanent ground deformation induced by explosive loading. Structural components are depicted as Lagrangian elements characterized by appropriate plasticity and damage models(Jablonski et al., 2012). The CEL method works best for carefully looking at the very nonlinear responses, big changes, material degradation, and interface interactions that happen when explosive forces are close by. Numerical models created with this technology are very useful for engineering design because they can predict how structures will behave under explosive loads and find possible failure modes. This method can be used for more than just explosions; it can also be used for a number of geotechnical problems, such as water-structure interaction, pile extraction, and slope stability in soft soils. This study developed a nonlinear dynamic finite element model employing the Coupled Eulerian-Lagrangian methodology in ABAQUS/Explicit software version 6.14-5. The Eulerian domain used for explosion simulations is two-dimensional and measures 16 m × 20 m × 0.01 m (Figure 12). The CEL methodology combines Lagrangian and Eulerian mesh generation algorithms to stop mesh deformation that could happen during an explosion. In the CEL model, the Lagrangian framework is located within the Eulerian domain, which is an unoccupied area before analysis(Mougeotte et al., n.d.). The size of the Eulerian domain was chosen so that pressure waves from the explosive charge could travel freely, so that boundary reflections could be reduced, and so that the numerical model could be calibrated to match physical reality. The area of 16 m (width) × 20 m (length), which corresponds to a designated loading condition of 0.5448 m² explosive area, was chosen as the smallest area that would ensure that shock waves and particle movements from the explosion die down before they reach the Eulerian bounds. In the case of the large explosive area (14 m²), the dimensions were changed to 80 m (width) × 100 m (length) using the linear scaling method to keep the same physical propagation and border ineffectiveness criteria. This method follows the TM 5-1300 and UFC 3-340-02(Criteria(UFC), 2008) guidelines that have been suggested in the literature for modeling how explosive products and pressure waves spread naturally while reducing the effects of artificial boundaries. The Eulerian mesh spacing was increased from 0.1 m to 0.5 m in the 14 m² load case, keeping the linear scale in relation to the 0.5448 m² reference. Localized refinement was done around the load and at the ground–air interface to make sure there were at least 20–30 elements per effective diameter and 15 elements per crater depth.

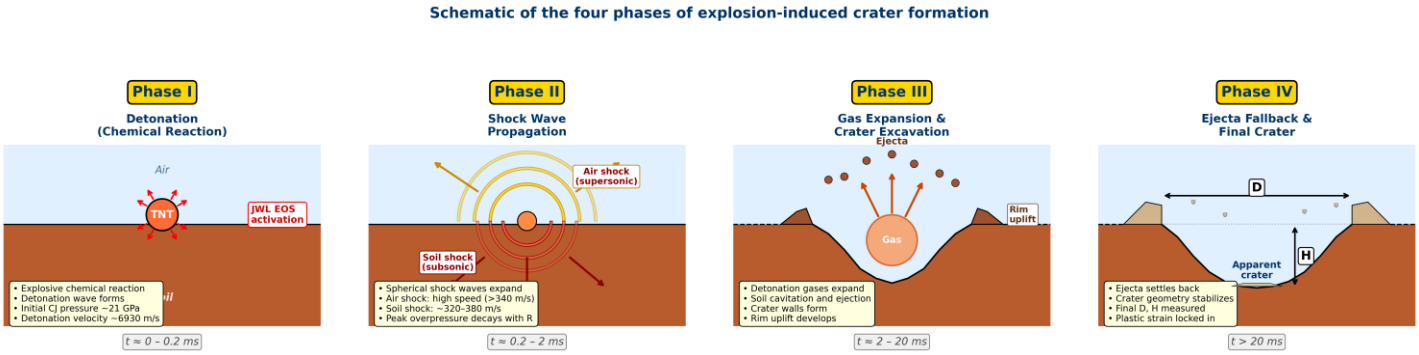


**Figure 11** Schematic representation of the four phases of explosion-induced crater formation: (I) Detonation and chemical reaction (0–0.2 ms), where the JWL equation of state governs the release of detonation energy at CJ pressure ~21 GPa and detonation velocity ~6930 m/s; (II) Shock wave propagation (0.2–2 ms), with supersonic air shock and subsonic soil shock expanding spherically from the source; (III) Gas expansion and crater excavation (2–20 ms), where the expanding detonation gases displace soil material outward and upward, creating the apparent crater and ejecting fragments; (IV) Ejecta fallback and final crater formation (>20 ms), in which the geometry stabilizes and the final crater dimensions (D, H) are established.

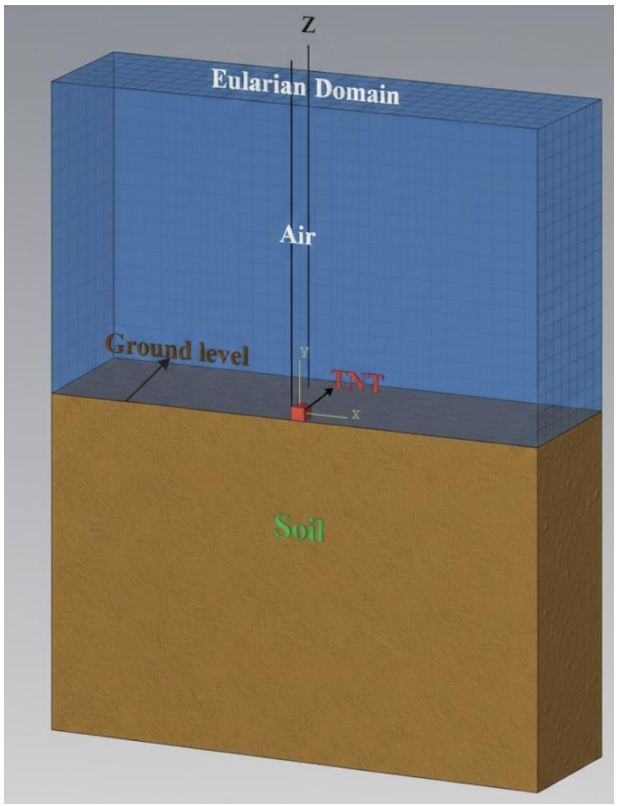


**Figure 12** 16x20m and 80x100m Eulerian Domains

### 3.1 Material Model and Parameters

#### 3.1.1 Air

The air model was created in ABAQUS using the ideal gas equation(Hodge & Koenig, 1995). The gas model is based on thermodynamic principles. This model provides computational efficiency in representing the behavior of air under varying pressure, density, and temperature conditions. The ideal gas equation is widely used in compressible air flow analysis due to its ability to define the thermodynamic relationship between pressure, density, and internal energy, and is suitable for modeling the propagation of sudden shock waves, such as explosions. In this formula (4), $P_A$ represents the ambient pressure, $R$ represents the specific gas constant, $\theta$ represents the flow temperature , and $\theta_Z$ represents absolute zero on the temperature scale. This is because specifying the specific heat for an ideal gas is required in constant-volume branches. As seen in equations 4 and 5 in the current model, specific heat at constant pressure has been included in the calculation. The value of the gas constant $R$may be reasonably approximated based on the thermodynamic state of the gas, such as its pressure and temperature, without introducing significant loss of accuracy in explosion-related simulations.The ideal gas approximation is adequate in areas where this value remains constant(N. M. Nagy, 2015) .The characteristics of air are presented in Table 7(Batchelor, 2000).

$$P + P_A = \rho R(\theta - \theta^Z) \tag{4}$$

$$R = c_p - c_v \tag{5}$$

**Table7** Air constants(Batchelor, 2000)

| | |
|---|---|
| Gas constant, $R$ | 287 J/kg/K |
| Ambient pressure $P_A$ | 101 kPa |
| Specific heat | 718 J/kg/K |
| Reference density | 1.225 kg/m$^3$ |
| Reference temperature | 15 ◦C |
| Dynamic Viscosity | 1.85E-005 (N. s/m$^2$) |

**3.1.2 Explosive**

The Jones-Wilkins-Lee (JWL) model is a prevalent Equation of State (EOS) used for the characterization of TNT explosives(Farag & Chinnayya, 2024; Z. Wang et al., 2004). Analyzing complicated explosion situations generally necessitates sophisticated computing techniques, including multi-material Eulerian and coupled Eulerian-Lagrangian (CEL) analysis, utilizing the Jones-Wilkins-Lee (JWL) equation of state to represent the explosive material. (Giam et al., 2020). The Jones–Wilkins–Lee (JWL) equation of state is recognized as the most effective for calculations in explosive dynamics(Lee, E.L.; Hornig, H.C.; Kury, 1968). The JWL EOS is an empirical correlation introduced by Jones, Miller, and Wilkins(Goswami et al., 2022; L. Liu et al., 2020; J. Wang et al., 2020; Xie et al., 2017), (Equation 6) can be articulated in isentropic form as follows:

$$P = A\left(1 - \frac{\omega}{R_1 V}\right)e^{-R_1 V} + B\left(1 - \frac{\omega}{R_2 V}\right)e^{-R_2 V} + \frac{\omega(\mathrm{E} + \mathrm{Q})}{V} \quad (6)$$

where A, B, $R_1$,$R_2$, and ω are material constants; $P_{cj}$ is the pressure of the detonation products, in GPa; V is the relative volume of the explosive product; and $e_0$ is initial specific internal energy, KJ/m$^3$. The JWL parameters listed in Table 8, together with the Chapman–Jouguet detonation pressure ($P_{cj}$), were adopted from the standard TNT values reported by Dobratz & Crawford (1985), which are widely accepted in the explosive dynamics literature. The constants in Table 8 were used in the modeling based on TNT equivalence.

**Table8** TNT constants(Dobratz & Crawford, 1985)

| Detonation wave speed-Cd(m/s) | $P_{cj}$ (Gpa) | A (Gpa) | B (Gpa) | ω | $R_1$ | $R_2$ | Density (kg/m$^3$) | $e_0$ (KJ/m$^3$) |
|---|---|---|---|---|---|---|---|---|
| 6930 | 21.0 | 373.8 | 3.747 | 0.35 | 4.15 | 0.9 | 1,023E+03 | 6,0E+06 |

**3.1.3 Soil**

The Mohr-Coulomb plasticity model was utilized in the investigation of the ground subjected to surface blasting. The MC model represents an optimal elastic-plastic structure(Xiang & Zi-Hang, 2017). In the MC model, damage is determined by the maximum shear stress and normal stress (Equation 7)(Rais et al., 2025). Fracture, as per the MC criterion at the failure point, is dictated by the maximum shear stress and is contingent upon the normal stress. This can be exemplified by constructing a Mohr circle based on the maximum and minimum principal stresses corresponding to the stress states at the failure site. The yield criterion of the Mohr-Coulomb model,

$$\tau = c + tan \tag{7}$$

Here, τ represents shear stress, σ represents normal stress, and c and ϕ represent cohesion and internal friction angle, respectively. Three stress invariants have been formulated for a model of the general stress state (Equation 8-15),

$$F = R_{mc}q - ptan\emptyset - c = 0 \tag{8}$$

$$R_{mc}(\theta, \emptyset = \frac{1}{\sqrt{3}cos\emptyset}\sin\left(\theta + \frac{\pi}{3}\right) + \frac{1}{3}\cos\left(\theta + \frac{\pi}{3}\right)tan\emptyset \tag{9}$$

$$\cos(3\theta) = (\frac{r}{q})^3 \tag{10}$$

$$p = -\frac{1}{3}trace(\sigma) \tag{11}$$

$$\cos(3\theta) = (\frac{r}{q})^3 \tag{12}$$

$$q = \sqrt{\frac{1}{3}(S:S)} \tag{13}$$

$$\mathrm{r} = (\frac{9}{2}S * S:S)^{\frac{1}{3}} \tag{14}$$

$$\mathrm{S} = \sigma + \mathrm{pl} \tag{15}$$

Where, τ represents shear stress, σ denotes normal stress, c and ϕ Regarding cohesiveness and the angle of internal friction, respectively. Three stress invariants have been formulated for a model of the general stress state: Where, θ denotes the deviatoric polar angle, p represents equivalent pressure stress, q signifies the von Mises equivalent stress, r indicates the third invariant of deviatoric stress, and S refers to deviatoric stress. The properties of the ground where the explosion occurred(Bhowmik et al., 2013, 2016; Keskin et al., 2022; Z. Wang et al., 2005) are given in Table 9.

**Table9** Soil constants(Bhowmik et al., 2013, 2016; Keskin et al., 2022; Z. Wang et al., 2005)

| Elastic | Poisson ratio | Friction Angle | Dilation angle | Cohesion Yield stress | Abs plastic strain | Density (kg/m^3) |
|---|---|---|---|---|---|---|
| 5,00E+07 | 3,00E-01 | 2,40E+01 | 1,20E-01 | 1,00E+05 | 0,00E+00 | 2,20E+03 |

### 3.1.4 Model Validation

In 2016, two distinct models were developed to mimic experimental explosions with 1, 2, and 3 kg of TNT equivalent explosives at a site near the location of the law enforcement attack, sharing identical ground characteristics. Two distinct domain areas were delineated for these models. A region measuring 16 × 20 m was designated for the simulation of experimental explosions, while an area measuring 80 × 100 m was allocated for the simulation of the security attack. An refined mesh was used to ensure the consistency of experimentally obtained crater geometries. To examine mesh sensitivity, calculations were performed using meshes with sizes of 0.025, 0.050, 0.075, 0.100, 0.125, 0.150, 0.175, and 0.200 m. As shown in Figure 13, the mesh size closest to the experimental measurements was determined to be 0.1 m. Since the same method will be used for explosions of other sizes, a sensitivity analysis was performed on a unit basis for 1 kg of explosive. In large-scale explosions, a coarse mesh was applied, particularly in the 80x100 m model. Here too, a sensitivity analysis was performed with mesh sizes of 0.10 m, 0.30 m, and 0.70 m (Fig. 14). Mesh seeding was applied uniformly along the domain boundaries to preserve regular element distribution and numerical stability. Boundary conditions were imposed to prevent rigid-body motion and to maintain numerical stability during the explicit dynamic solution. Specifically, displacement constraints were applied at the far-field boundaries consistent with Equations 16-18, while allowing the internal domain to deform freely under blast loading. In the Eulerian domain, the initial material distribution was defined using volume fractions such that the sum of the air, soil, and explosive fractions within each Eulerian element satisfied the CEL requirement of unity. Each material region was defined as a separate set, and the corresponding air/soil/TNT volume fractions were assigned accordingly (Table 10). To improve numerical robustness, the total assigned volume fraction was set slightly below 1.0.

$$U_x = U_y = U_z = U_{rx} = U_{ry} = U_{rz} = 0 \tag{16}$$

$$U_x = U_{\mathrm{ry}} = U_{\mathrm{rz}} = 0 \tag{17}$$

$$U_z = U_{\mathrm{rx}} = U_{\mathrm{ry}} = 0 \tag{18}$$

**Table10** Volume fractions

| Region | Air | Soil | Tnt | Void |
|---|---|---|---|---|
| Domain-1.Air | 1 | 0 | 0 | 0 |
| Domain-1.Soil | 0 | 1 | 0 | 0 |
| Domain-1.Tnt | 0 | 0 | 1 | 0 |

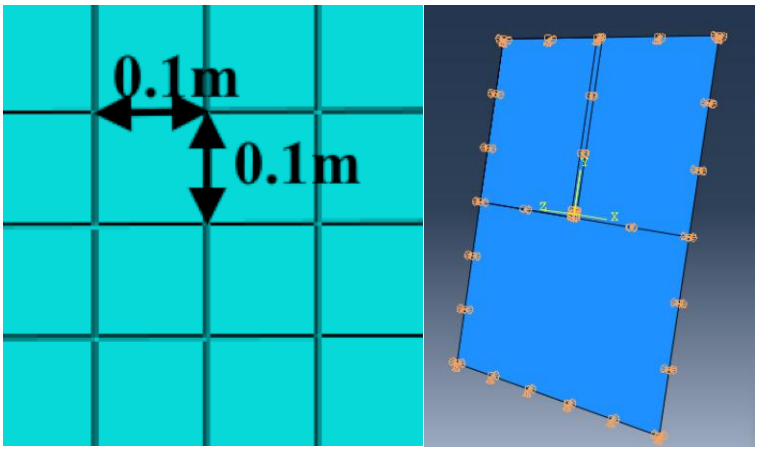


**Figure 13** Experimental model mesh sizes and structural bearing conditions

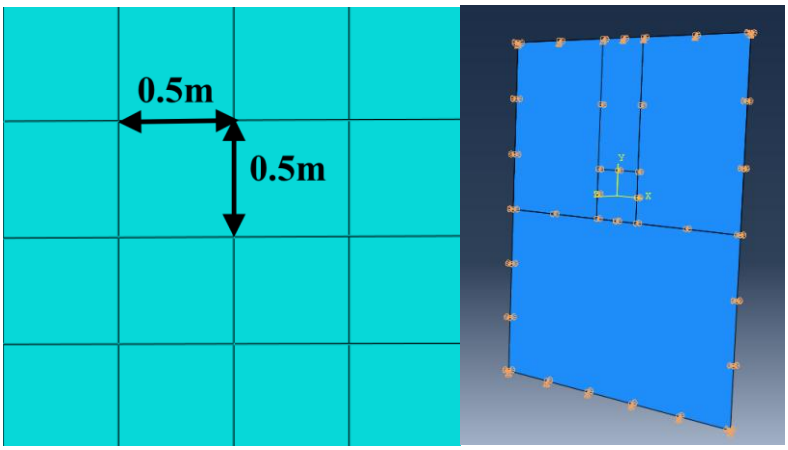


**Figure 14** Numeric model mesh sizes and structural bearing conditions

### 3.2. Experimental and Model Discussion

Crater dimensions ($D_{avg}$ and $H_{avg}$) reported in this study were extracted directly from the deformed CEL mesh in ABAQUS/Viewer (version 6.14-5) using the Probe Values tool, by querying the nodal coordinates corresponding to the rim crest peaks on both sides of the crater and the deepest point of the crater along the central cross-section. The crater dimensions are reported using the apparent crater convention widely adopted in the cratering literature (Kinney & Graham, 2013), in which $D_{avg}$ is measured as the horizontal distance between the rim crest peaks, and $H_{avg}$ is the vertical distance from the rim crest level down to the crater bottom. For small-scale explosions (1, 2, and 3 kg TNT-equivalent cases), the uplifted rim is minor ($\Delta H \ll H$), so the apparent crater depth closely coincides with the depth measured from the original ground surface (the $H_1$ definition in Figure 8). For the large-scale 1983 kg event, however, the rim uplift is significant due to the much greater explosive energy and the larger volume of ejected material; consequently, in Figure 21, both the original ground surface (dashed line) and the rim crest level (the reference for $H_{avg}$) are explicitly shown for clarity. The blast index n = (D/2)/H is computed using the same H definition across all cases to ensure scale-to-scale consistency. For visualization purposes, the reference lines and the $D_{avg}$, $H_{avg}$ measurement arrows shown in Figures 15, 17, 19, and 21 were overlaid on the EVF contour plots in post-processing, based on the numerical values obtained from the direct nodal coordinate queries.

There is a clear agreement between field explosion tests and computer simulations when it comes to the size and depth of craters made by a 1 kg TNT equivalent explosive. The average diameter of the craters was $D_{avg}$ 2.1 m, and the average depth was $H_{avg}$ 0.70 m (Figure15). The experimental measurements yielded D = 2.15 m and H = 0.65 m, exhibiting a discrepancy of less than 5%. The H/D ratio is 0.30 in both cases, which is consistent with what is known about small-scale surface explosions(Ambrosini et al., 2002; Ambrosini & Luccioni, 2006; Criteria(UFC), 2008). This situation illustrates that the established CEL-based model effectively encapsulates the geometric similarity. The Eulerian Volume Fraction (EVF) distribution distinctly illustrates the material displacement and void creation during crater development. Red areas (EVF = 1.0) indicate cells entirely occupied by soil, whereas blue areas signify soil expulsion and the creation of voids. Moreover, equivalent plastic strain (PEEQ) contours indicate elevated plastic strain regions at the crater peripheries, but the PE22 (equivalent plastic strain component in the 2–2 direction) distribution illustrates stress strain at the crater borders and significant compression behavior at the core . Analysis of the vertical displacement (U2) contour maps shows that, small-scale tests (Figures 16, 18, and 20),, deformation is primarily concentrated along the crater edges and gradually decreases toward the surrounding ground. A similar response pattern was observed in the small-scale experiments, where the highest vertical displacements occurred near the crater center and rim regions for the 1 kg and 2 kg charges, while areas farther from the crater remained largely unaffected. This behavior indicates that a significant portion of the explosive energy is consumed during crater formation and soil ejection, resulting in limited deformation at greater distances. For the 2 kg charge case, the crater diameter was measured as $D_{avg} = 3.0$m and its height as $H_{avg} = 0.91$m (Figure 17). The pressure generated by the explosion spread across the ground, causing volumetric displacement, resulting in stress accumulations at the crater edges. Stress accumulation occurred at the crater edge (Figure 18). When the explosive charge was increased to 3 kg, the crater diameter increased to 3.70 m, while its height rose to 1.05 m (Figure 19). Examining the crater geometry revealed material accumulation at the crater edges due to volumetric displacement and soil ejection during the explosion. High PEEQ values were obtained around the crater. This showed that permanent deformation reached its maximum level under this loading condition (Figure 20). When examining the PE22 distributions (Figure 20b), significant stress accumulations are observed beneath the core region of the crater. With the increase in explosive weight, horizontal and vertical displacements increased significantly, and deformation intensified from the blast point toward the crater floor. It was observed that as the explosive weight increased, the crater dimensions increased at a non-linear rate both crater diameter (D) and depth (H) increase nonlinearly with explosive mass, while the H/D ratio remains nearly constant at approximately 0.30 for the small-scale cases, indicating geometric similarity at this scale. The variation of the blast index between 1.57 and 1.79 confirms the joint development of the blast index and the soil ejection intensity. The CEL approach developed in this study successfully completes crater formation based on explosion indices using JWL state equations and the Mohr-Coulomb model. The data obtained can provide reliable net crater dimensions for different explosive charges and different ground conditions, while field simulations facilitate forensic analysis.

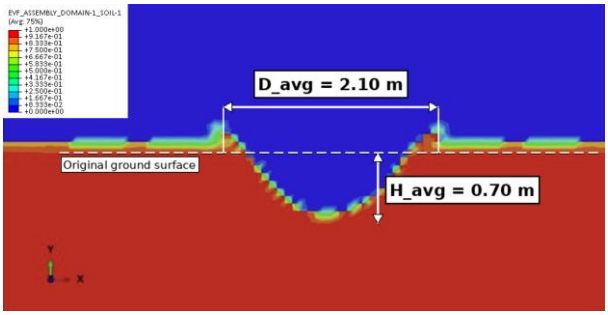


**Figure 15** Comparison of the crater formed by the CEL analysis with the experimental crater for 1 kg of explosive

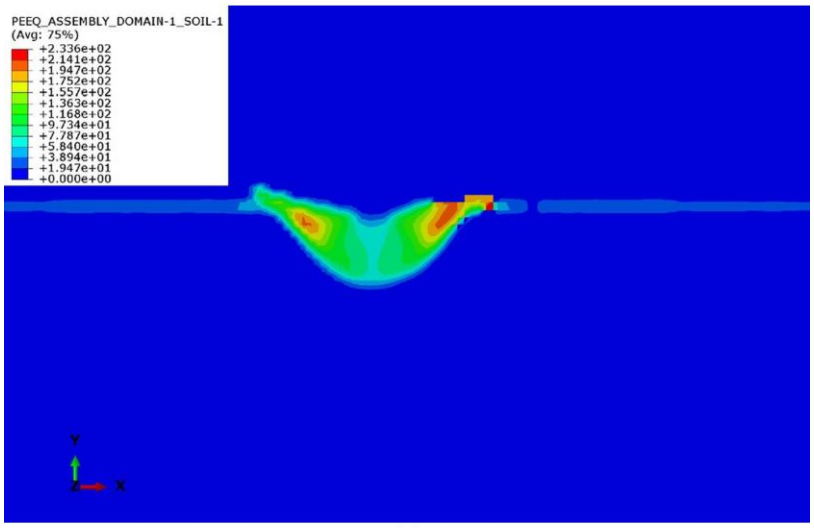


(a)

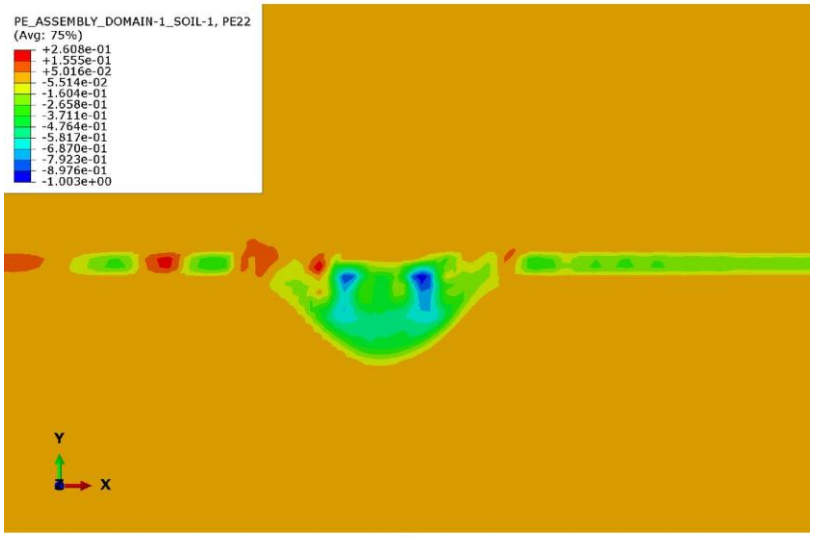


(b)

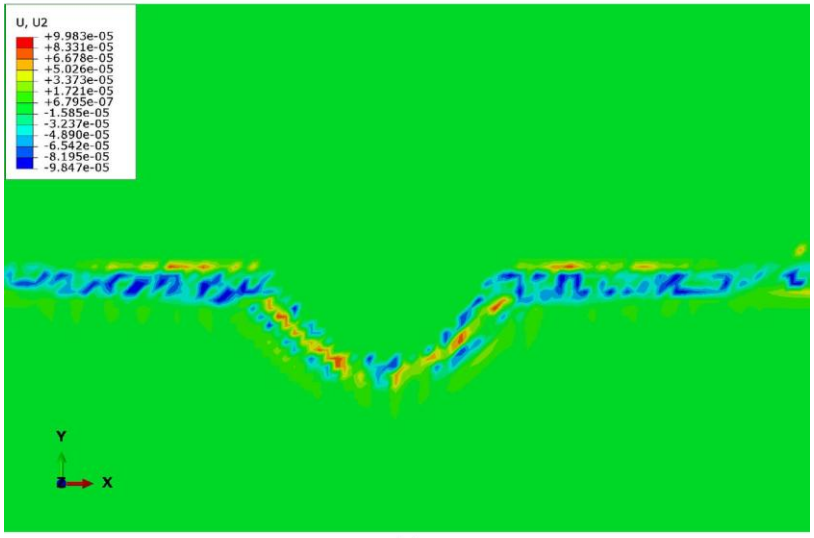


(c)

**Figure 16** Contour distributions of (a) equivalent plastic strain (PEEQ), (b) plastic strain component PE22, and (c) vertical displacement $U_2$ for the 1 kg TNT equivalent surface contact explosion at the final analysis step.

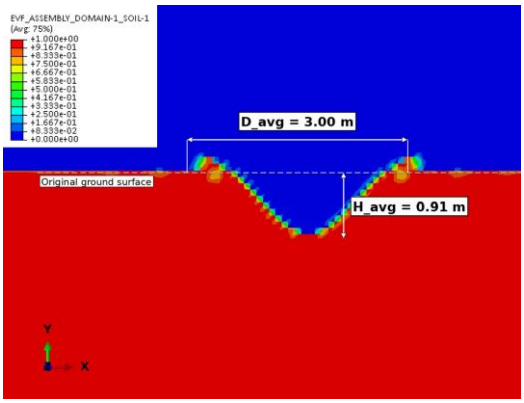


**Figure 17** Comparison of the crater formed by the CEL analysis with the experimental crater for 2 kg of explosive

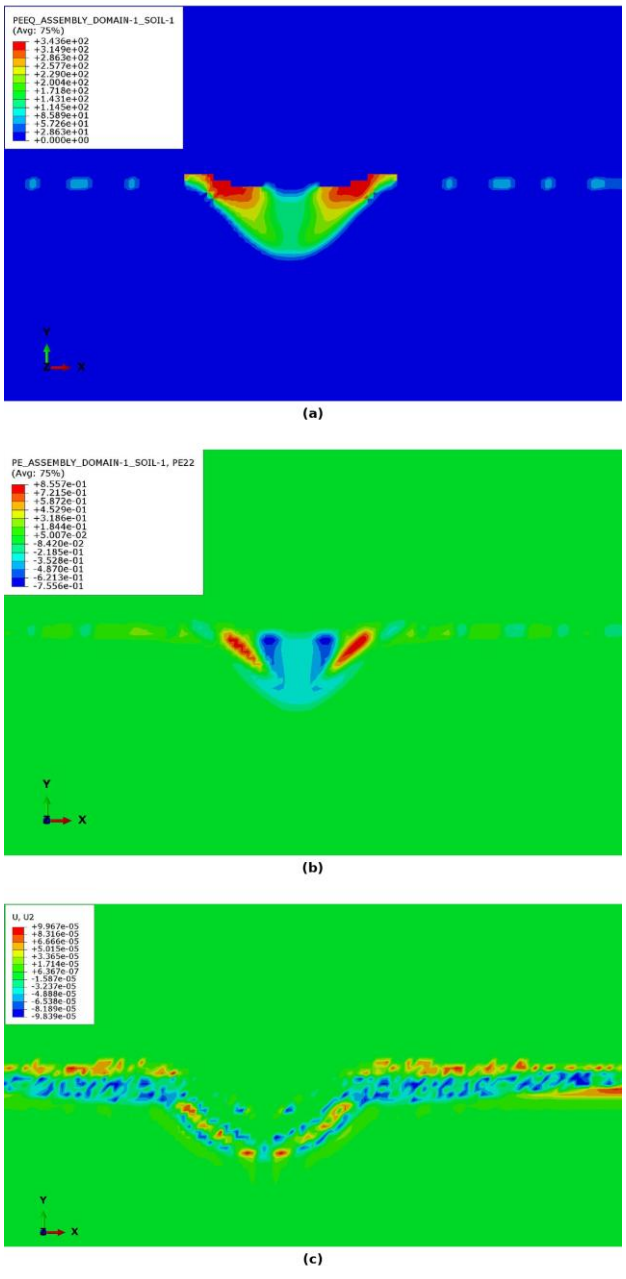


**Figure 18** Contour distributions of (a) equivalent plastic strain (PEEQ), (b) plastic strain component PE22, and (c) vertical displacement $U_2$ for the 2 kg TNT equivalent surface contact explosion at the final analysis step.

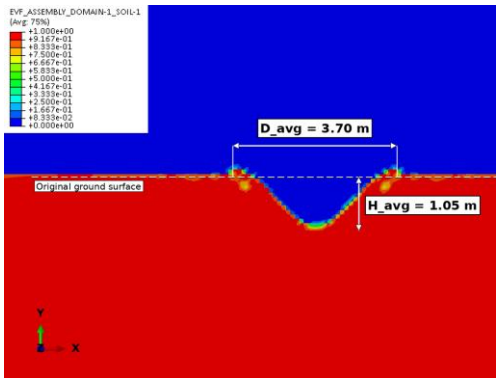


**Figure 19** Comparison of the crater formed by the CEL analysis with the experimental crater for 3 kg of explosive

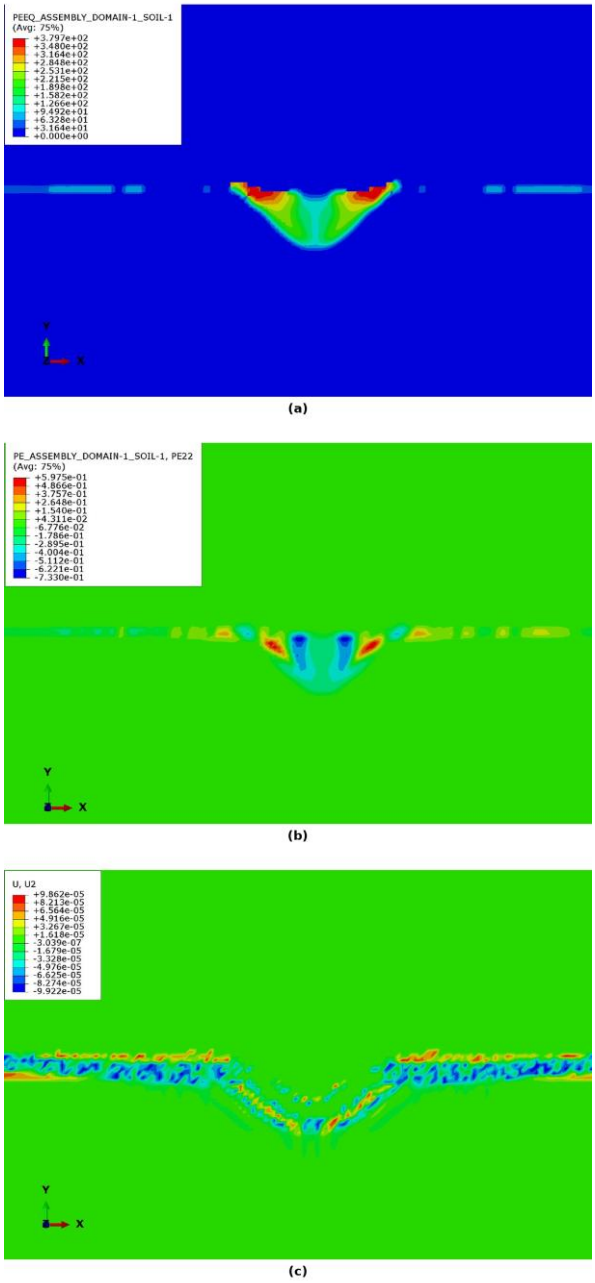


**Figure 20** Contour distributions of (a) equivalent plastic strain (PEEQ), (b) plastic strain component PE22, and (c) vertical displacement $U_2$ for the **3 kg TNT-equivalent** surface contact explosion at the final analysis step.

### 3.2.1. Large-scale forensic application: the 1983 kg vehicle-borne explosion

This study quantitatively examined the crater geometry produced by the 2016 vehicle bomb attack in Elazığ, Turkey, utilizing approximately 2 tons of TNT-equivalent explosive material, through a Coupled Eulerian–Lagrangian (CEL)-based computational model specifically designed for this analysis. Field studies found that the crater was about 10 m wide and 5 m deep, which gave it a height-to-diameter ratio (H/D) of about 0.50 and a blast index value (n) of about 1 (Figure 21). The average crater size from the numerical simulation was $D_{avg}$ = 10 m and $H_{avg}$ = 5 m. The difference between the field measurements and the numerical predictions was less than 8% for both diameter and depth. These results show that the numerical model we made accurately reflects what we saw in the field. The Eulerian Volume Fraction (EVF) distributions derived from the simulation indicate that both the crater void geometry and the volume of ejected material align with field observations (Figure 22). The symmetric upward movement of the crater walls on both sides of the explosion center shows that the material ejection mechanism is the same on both sides. The equivalent plastic strain (PEEQ) contours show that the worst permanent deformations happened along the slopes and rim of the crater, where shear-dominated failure mechanisms were most common. The PE22 strain component, on the other hand, shows that tensile stresses were mostly found around the edges of the crater, while compressive stresses were mostly found below the explosion core. The resulting uneven strain distribution is closely linked to the upward soil ejection and crater void formation that were observed during the field studies. The simulation of the large-scale explosion equivalent to 1983 kg of TNT produced vertical displacement ($U_2$) patterns with maximum values at the center of the crater and values that gradually decreased toward the edges of the crater. At the point of detonation, the highest vertical displacements were found. The displacement levels around it are clearly similar. The deformations formed in the crater's deformation bands show an even distribution on the ground. The fact that the displacements recorded in small-scale explosions are less can be evaluated based on the coarse mesh density applied in large-scale explosions. Furthermore, the pressure from the explosion spreading over a wider area is responsible for reducing the displacement amplitudes. When the numerical results are examined, the D/H ratio in large-scale explosions is in the range of 1.80-2.20, confirming that it has a wide and shallow crater. The fact that this ratio is approximately 0.30 in the small-scale tests and 0.50 in the large-scale 1983 kg case confirms the accuracy of the scaling, the experimental and numerical consistency, and the possibility of integrating it into explosion-induced crater formation. The developed numerical model accurately represents the essential geometric parameters (D, H, n) and the principal zones of ground deformation. A direct comparison of field experiments and numerical results shows that the crater diameter (D) and depth (H) are very similar (Figure 23). The diameter predictions are very similar, with a root mean square error (RMSE) of 0.20 m, which shows that they are very accurate. There is a slightly bigger difference in crater depth, with an RMSE of 0.40 m. This is mostly because the numerical model predicts depths that are a little deeper than those measured in the field, especially for the large-scale explosion case. Still, the differences in crater diameter and depth are still within acceptable limits for engineering uses. Also, the fact that the diameter–depth relationship shows the same trends at different scales shows that the numerical model accurately shows how the field behaves as the explosive charge increases. Since predicting crater depth is usually harder than predicting diameter, the level of agreement that was reached supports the CEL-based modeling approach's strength and dependability even more. In conclusion, the small differences between field measurements and numerical predictions show that the CEL model is a valid and reliable way to show how craters form from both small and large surface explosions. The suggested modeling framework can thus be reliably utilized in forthcoming blast effect evaluations, forensic investigations, and the engineering of protective and blast-resistant edifices. For full reproducibility, the complete set of modeling parameters employed in this large-scale forensic CEL simulation is summarized in Table 11. The combination of these parameters yielded predicted crater dimensions of $D_{avg} \approx 10$ m and $H_{avg} \approx 5$ m (with the 0.5 m mesh size), in close agreement with the field-measured values (D = 10 m, H = 5 m; relative error < 8%).

**Table11** Summary of key modeling parameters for the 1983 kg TNT-equivalent forensic CEL simulation.

| Component | Parameter | Value | Reference |
|---|---|---|---|
| Eulerian domain | Dimensions | 80 × 100 × 0.01 m | This study |
| | Mesh size | 0.5 m | This study |
| Soil(Mohr–Coulomb) | Cohesion, c | 100 kPa | Keskin et al., 2022 |

| | | | |
|---|---|---|---|
| | Friction angle, ϕ | 24° | Keskin et al., 2022 |
| | Dilation angle, ψ | 0.12° | Keskin et al., 2022 |
| | Elastic modulus, E | 50 MPa | Keskin et al., 2022 |
| | Poisson ratio, ν | 0.30 | Keskin et al., 2022 |
| | Density, ρ | 2200 kg/m³ | This study |
| TNT (JWL EOS) | $C_d$ | 6930 m/s | Lee et al., 1968 |
| | $P_{CJ}$ | 21 GPa | Dobratz&Crawford,1985 |
| | A | 373.8 GPa | Lee et al., 1968 |
| | B | 3.747 GPa | Lee et al., 1968 |
| | $R_1$ | 4.15 | Lee et al., 1968 |
| | $R_2$ | 0.9 | Lee et al., 1968 |
| | ω | 0.35 | Lee et al., 1968 |
| | Density, ρ | 1023 kg/m³ | Dobratz&Crawford,1985 |
| | $e_o$ | $6.0\times10^6$ kJ/m³ | Lee et al., 1968 |
| Air (Ideal gas) | R | 287 J/(kg·K) | Batchelor, 2000 |
| | $P_A$ | 101 kPa | Batchelor, 2000 |
| | $c_v$ | 718 J/(kg·K) | Batchelor, 2000 |
| | Density, ρ | 1.225 kg/m³ | Batchelor, 2000 |

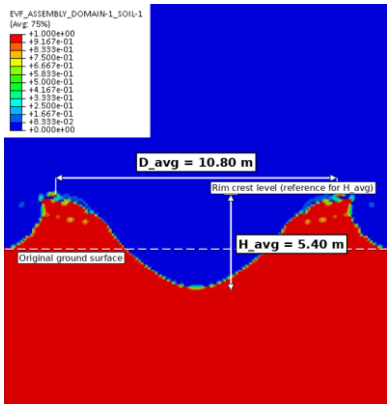


**Figure 21** Comparison of the crater formed by the CEL analysis with the experimental crater for 1983 kg of explosive

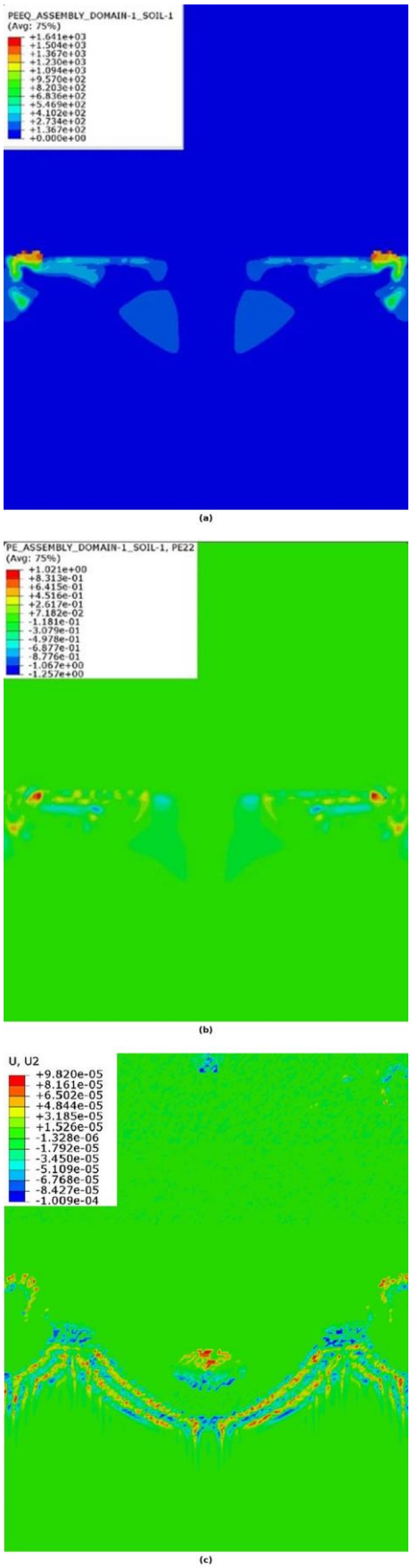


**Figure 22** Contour distributions of (a) equivalent plastic strain (PEEQ), (b) plastic strain component PE22, and (c) vertical displacement $U_2$ for the 198**3 kg TNT-equivalent** surface contact explosion at the final analysis step

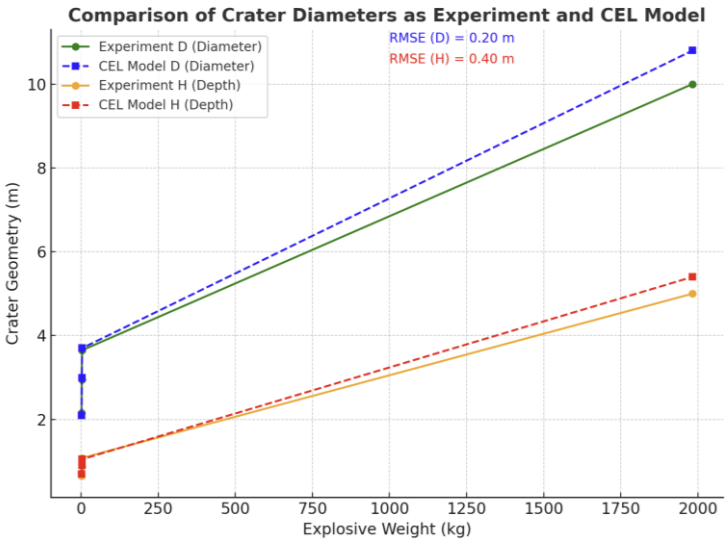


**Figure 23** Comparison of crater diameters as Field and Model

### 3.3. Mesh sensitivity analysis

The mesh sensitivity analysis in this study looked at how changing the sizes of the elements, which ranged from 0.025 m to 0.20 m, affected the predicted crater diameter ($D_{av}g$) and depth ($H_{av}g$).When compared with experimental data, fine meshes (0.025 m and 0.050 m) provide significant insights into both crater diameter and depth (Figure 24). It is observed that deformation of the crater region increases as a result of explosions in fine meshes. It should be noted that the agreement between the crater diameter and height and the experimental measurements increases for mesh sizes between 0.075 m and 0.125 m. In particular, the 0.10 m mesh size shows the closest agreement with the field data. In coarser meshes, the crater depth remains largely unchanged, while small increases in diameter are observed. This is because increasing the mesh size limits the resolution of deformation models and stress gradients that cause crater formation. Overall, the results obtained show that explosion-induced crater sizes are effective in investigating explosive ground interaction. As usual, fine meshes were more successful in stress distributions and even yielded better results than coarse meshes in crater geometry. The chosen mesh resolution is therefore very important for making sure that CEL-based blast simulations are both physically realistic and numerically stable. Quantitatively, the mesh convergence study confirmed that the variations in predicted crater diameter and depth remained within 5–10% across the converged mesh range (0.075–0.125 m for the small-scale model and 0.1–0.3 m for the large-scale model), demonstrating both numerical stability and convergence.

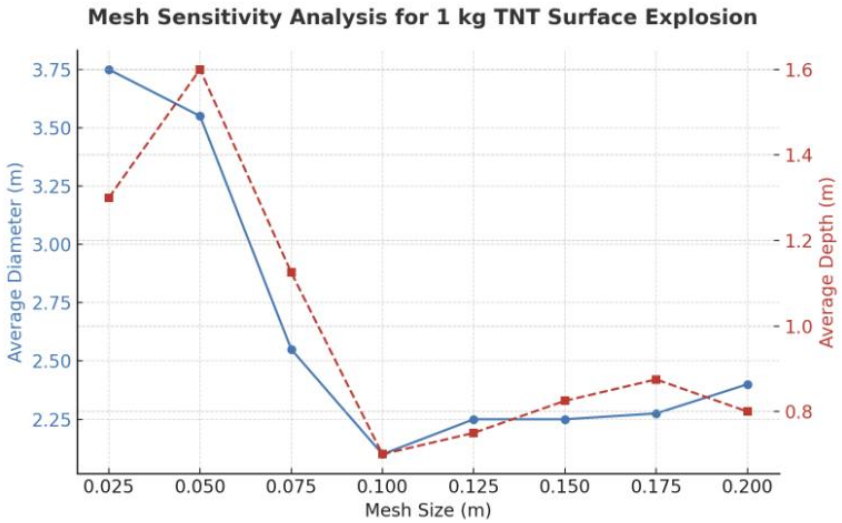


**Figure 24** Mesh sensitivity for Experimental

The mesh sensitivity analysis for the large-scale blast equivalent to 1983 kg of TNT shows that the predicted crater diameter and depth are similar for mesh sizes of 0.1 m and 0.3 m (Figure 25). When coarser mesh sizes of 0.5 m and 0.7 m are used, on the other hand, there are clear differences. The numerical model predicts that the average crater dimensions for a mesh size of 0.5 m are $D_{avg}$ =10 m and $H_{avg}$ =5 m. These numbers are very close to the field measurements of about 10 m in diameter and 5 m in depth. The finer mesh resolution of 0.1 m gives you more geometric detail, but it costs a lot more to compute. Taking into account the trade-off between accuracy and speed, a mesh size of 0.5 m was chosen as the best way to break up the large-scale explosion simulations. This choice provides a numerically stable solution that shows close agreement with field observations, while maintaining a reasonable balance between predictive accuracy and computational efficiency.

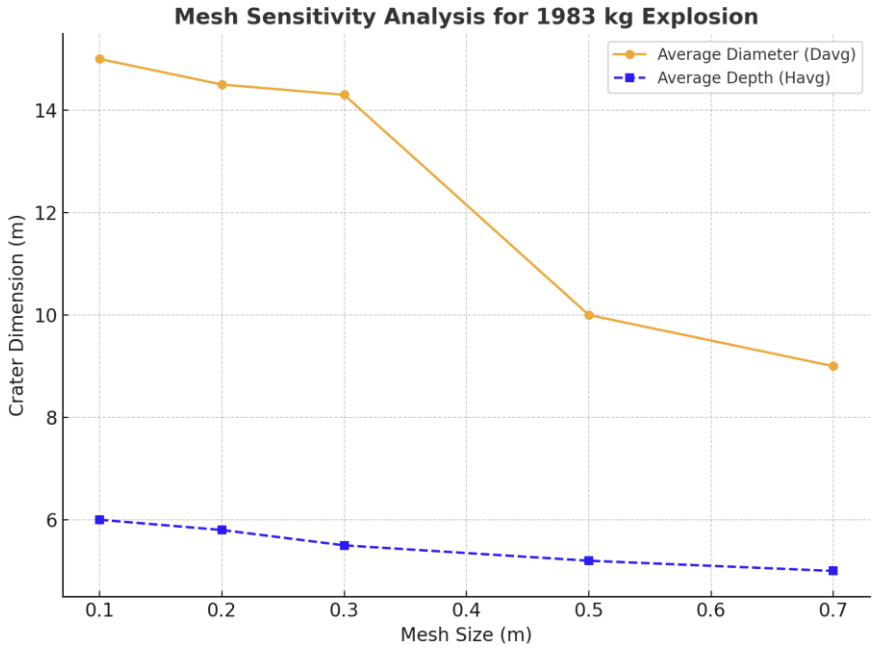


**Figure 25** Mesh sensitivity for 1983 kg explosion

The choice of the 0.5 m mesh for the large-scale (1983 kg) simulation was based primarily on field-validation accuracy rather than computational efficiency. As shown in Figure 25, the 0.5 m mesh predicts crater dimensions of $D_{avg}$ = 10 m and $H_{avg}$ = 5 m, which coincide exactly with the field measurements from the 2016 Elazığ vehicle-borne explosion. In contrast, the finer 0.3 m mesh overestimates the crater diameter, predicting $D_{avg}$ = 14.3 m and $H_{avg}$ =5.5 m a diameter overestimation of approximately 43% relative to the field-measured value. The recorded computational costs for the two meshes were modest and comparable (CPU time ≈ 20 s for the 0.3 m mesh vs. ≈ 25 s for the 0.5 m mesh; memory usage ≈ 100.7 MB for both, as obtained from the simulation status log files). Computational efficiency was therefore not the deciding factor in the mesh selection; the 0.5 m mesh was selected because it yielded the closest agreement with the field-measured crater geometry of the actual event being reconstructed. The finer 0.3 m mesh is acknowledged as numerically stable and remains valuable for analyses requiring higher fidelity in local stress and strain gradient distributions near the crater rim; however, for the primary forensic-reconstruction objective of this study, field-validation accuracy was prioritized.

### 3.4 Pressure-Time Response and Wave Propagation

To provide further insight into the dynamic response of the 1983 kg TNT-equivalent surface explosion, pressure-time histories were extracted from numerical gauge points at representative locations in the air and soil domains. The air pressure history was recorded at a horizontal distance of approximately 7.25 m from the blast center, while the soil pressure was sampled at three depths (0.5, 1.0, and 2.0 m) directly beneath the explosion center. The resulting pressure-time curves are presented in Figure 26. In the air (Figure 26a), the peak overpressure reached approximately 101 kPa at t ≈ 1.59 ms at the closest accessible Eulerian gauge point (approximately 7.25 m horizontal distance from the blast center). The relatively low overpressure at this gauge reflects the rapid spatial decay of the air shock with distance and the gauge's location outside the near-field region; the principal blast loading on the soil is captured by the subsurface gauges in panel (b). It should be noted that this peak value corresponds to the closest accessible Eulerian gauge point (approximately 7.25 m from the blast center) and therefore reflects the spatial decay of the air shock outside the near-field region. This pattern is consistent with the classical Friedlander pressure-time profile observed in free-field blast loading, where the initial shock front is followed by a slowly decaying positive overpressure phase. In the soil (Figure 26b), the pressure-time histories exhibit a clear progressive propagation pattern. The peak pressures recorded were 43.7 MPa at 0.5 m depth (arrival time 1.59 ms), 57.4 MPa at 1.0 m depth (1.89 ms), and 68.0 MPa at 2.0 m depth (2.55 ms). The systematic delay in arrival time with depth corresponds to a mean shock wave propagation speed of approximately 320-380 m/s through the cohesive soil medium, which is consistent with values reported in the literature for clay-rich soils (Henrych, 1979; Smith & Hetherington, 1994).The progressive increase in peak pressure with depth reflects the focusing of the soil shock wave in the near-source region, where the kinetic energy released by the detonation gas expansion is more efficiently confined by the surrounding soil mass — an effect commonly observed in contained or shallow-buried explosions (Adushkin & Khristoforov, 2004; Kinney & Graham, 2013). These pressure-time responses corroborate the plastic strain distributions presented in Figures 20 and 22, where the highest PEEQ and PE22 values were localized along the crater walls and the underlying soil column, confirming the consistency between the global crater geometry and the local stress-strain evolution captured by the CEL model.

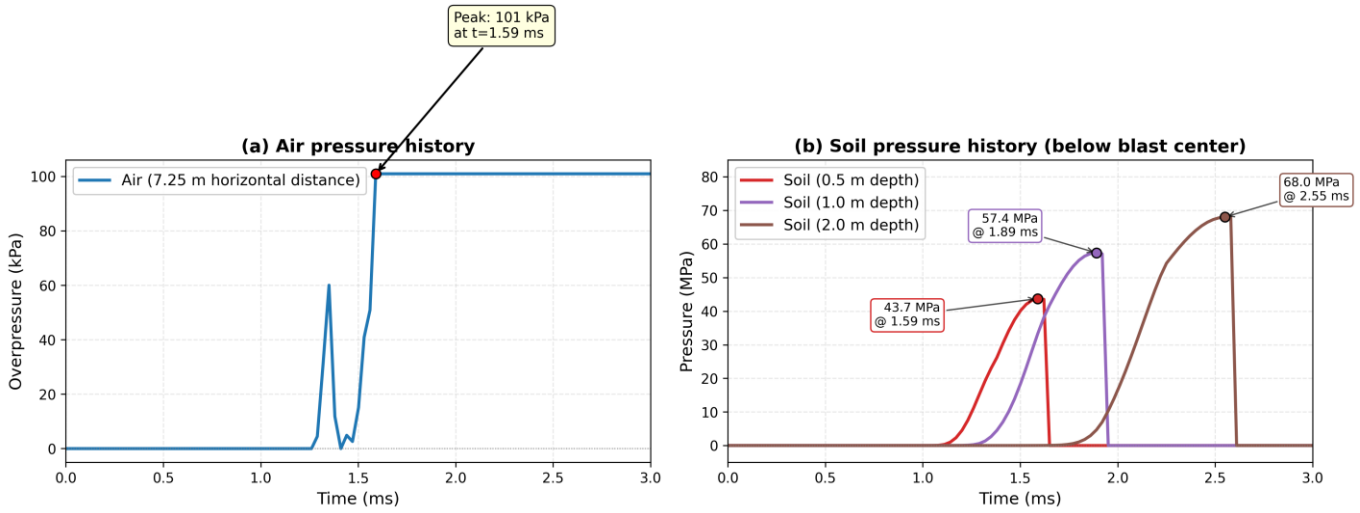


**Figure 26.** Pressure-time histories from the 1983 kg TNT-equivalent CEL simulation: (a) air overpressure at 7.25 m horizontal distance from the blast center; (b) soil pressure at three depths (0.5, 1.0, and 2.0 m) directly beneath the explosion center. Peak values are annotated with their arrival times. All curves correspond to the final analysis step of the simulation.

## 4 CONCLUSION

The current investigation developed and systematically evaluated a numerical modeling framework employing the Coupled Eulerian– Lagrangian (CEL) method in Abaqus/Explicit to simulate crater formation due to surface explosions. The model was calibrated through controlled field experiments using 1, 2, and 3 kg TNT- equivalent charges and then validated against a major vehicle- borne explosion in Elazığ, Turkey, in 2016, which involved about 2 tons of TNT equivalent. The findings indicate that the proposed CEL framework can precisely replicate crater geometry across three orders of magnitude in explosive mass. For small-scale explosion tests (1–3 kg TNT equivalent), the predicted and measured crater diameter and depth were less than 5% off, and the depth-to- diameter (H/D) ratios were close to 0.30. The difference between the numbers and the field results for the big field explosion was less than 8%, which is about 0.50 for the H/D ratio. These results clearly show a nonlinear scale effect. Larger explosives already create wider and deeper craters. However, the CEL model was found to be effective in determining crater geometry and size formation in explosions of different scales. This study, the first of its kind in the literature, will be particularly inspiring for forensic analysis in examining ground behavior and crater geometry and size in explosions of different magnitudes.

**Author's Contributions:** Conceptualization, Dbakır; Methodology, Dbakır; Investigation, Dbakır; Writing - original draft, Dbakır; Writing - review & editing Dbakır; Funding acquisition, Dbakır; Resources, Dbakır; Supervision, Dbakır.

**Data Availability:** Research data is only available upon request

**Editor:** Marcílio Alves

## References

Adushkin, V. V., & Khristoforov, B. D. (2004). Craters of Large-Scale Surface Explosions. *Combustion, Explosion and Shock Waves*, *40*(6), 674–678. https://doi.org/10.1023/B:CESW.0000048270.62239.01

Ambrosini, R. D., & Luccioni, B. M. (2006). Craters Produced by Explosions on the Soil Surface. *Journal of Applied Mechanics*, *73*(6), 890–900. https://doi.org/10.1115/1.2173283

Ambrosini, R. D., Luccioni, B. M., Danesi, R. F., Riera, J. D., & Rocha, M. M. (2002). Size of craters produced by explosive charges on or above the ground surface. *Shock Waves*, *12*(1), 69–78. https://doi.org/10.1007/s00193-002-0136-3

Bakır, D. (2025). Experimental and coupled Eulerian and Lagrangian numerical modeling of ground contact explosions. Firat University Journal of Experimental and Computational Engineering, 4(3), 618–636. https://doi.org/10.62520/fujece.1736569

Batchelor, G. K. (2000). *An Introduction to Fluid Dynamics*. Cambridge Un. Press.

Benson, D. J. (1992). Computational methods in Lagrangian and Eulerian hydrocodes. *Computer Methods in Applied Mechanics and Engineering*, *99*(2–3), 235–394. https://doi.org/10.1016/0045-7825(92)90042-I

Bhowmik, D., Baidya, D. K., & Dasgupta, S. P. (2013). A numerical and experimental study of hollow steel pile in layered soil subjected to lateral dynamic loading. *Soil Dynamics and Earthquake Engineering*, *53*, 119–129. https://doi.org/10.1016/j.soildyn.2013.06.011

Bhowmik, D., Baidya, D. K., & Dasgupta, S. P. (2016). A numerical and experimental study of hollow steel pile in layered soil subjected to vertical dynamic loading. *Soil Dynamics and Earthquake Engineering*, *85*, 161–165. https://doi.org/10.1016/j.soildyn.2016.03.017

Chen, J., Newlin, J. A., Zhang, H., Hu, S., & Luo, M. (2019, April 26). Large Deformation Finite Element Analysis of Riser-Soil Interactions with Strain-Softening Soils. *Offshore Technology Conference*. https://doi.org/10.4043/29376-MS

Cooper, P. W. (1994). Comments on TNT Equivalence. *Presented at the 20th International Pyrotechnics Seminar*.

Criteria(UFC), U. F. (2008). Structures to Resist the Effects of the Accidental Explosions. In *Department of Defence,United States of America*. https://doi.org/10.31142/ijtsrd23455

Defense, D. of. (2008). UFC 3-340-02. Structures to resist the effects of the accidental explosions. *Unified Facilities Criteria*, *December*, 1943.

*Dobratz, B. M., & Crawford, P. C. (1985). LLNL Explosives Handbook: Properties of Chemical Explosives and Explosive Simulants. Lawrence Livermore National Laboratory, Report UCRL-52997.*

Dolatshahi, A., & Qarahasanlou, A. N. (2023). Pre-existing Crack Effect on Damage of Inner Concrete Lining under an Internal Explosion: A Numerical Study. *Journal of Mining and Environment*, *14*(3), 945–960. https://doi.org/10.22044/jme.2023.12682.2304

Dolejš, M., Pacina, J., Veselý, M., & Brétt, D. (2020). Aerial Bombing Crater Identification: Exploitation of Precise Digital Terrain Models. *ISPRS International Journal of Geo-Information*, *9*(12), 713. https://doi.org/10.3390/ijgi9120713

Edri, I. E., Grisaro, H. Y., & Yankelevsky, D. Z. (2019). TNT equivalency in an internal explosion event. *Journal of Hazardous Materials*, *374*, 248–257. https://doi.org/10.1016/j.jhazmat.2019.04.043

Esparza, E. D. (1986). Blast measurements and equivalency for spherical charges at small scaled distances. *International Journal of Impact Engineering*, *4*(1), 23–40. https://doi.org/10.1016/0734-743X(86)90025-4

Fang, Z., Huang, J., Huang, Z., Chen, L., Cong, B., & Yu, L. (2020). An earthquake casualty prediction method considering burial and rescue. *Safety Science*, *126*, 104670. https://doi.org/10.1016/j.ssci.2020.104670

Farag, G., & Chinnayya, A. (2024). On the Jones-Wilkins-Lee equation of state for high explosive products. *Propellants, Explosives, Pyrotechnics*, *49*(3). https://doi.org/10.1002/prep.202300223

Formby, S. A., & Wharton, R. K. (1996). Blast characteristics and TNT equivalence values for some commercial explosives detonated at ground level. *Journal of Hazardous Materials*, *50*(2–3), 183–198. https://doi.org/10.1016/0304-3894(96)01791-8

Giam, A., Toh, W., & Tan, V. B. C. (2020). Numerical Review of Jones–Wilkins–Lee Parameters for Trinitrotoluene Explosive in Free-Air Blast. *Journal of Applied Mechanics*, *87*(5). https://doi.org/10.1115/1.4046243

Goswami, A., Ganesh, T., & Das, S. (2022). International Journal of Impact Engineering RC structures subjected to combined blast and fragment impact loading : A state-of-the-art review on the present and the future outlook. *International Journal of Impact Engineering*, *170*(July 2021), 104355. https://doi.org/10.1016/j.ijimpeng.2022.104355

Grisaro, H. Y., & Edri, I. E. (2017). Numerical investigation of explosive bare charge equivalent weight. *International Journal of Protective Structures*, *8*(2), 199–220. https://doi.org/10.1177/2041419617700256

Henrych, J. (1979). The dynamics of explosion and its use. Elsevier, Amsterdam.

Hodge, B. K., & Koenig, K. (1995). *Compressible Fluid Dynamics with Personal Computer Applications.* Prentice Hall.

Hussein, A., & Heyliger, P. (2025a). Blast Pressure Simulation of a Suicide Vest Attack. *Diyala Journal of Engineering Sciences*, *18*(1), 249–258. https://doi.org/10.24237/djes.2025.18115

Hussein, A., & Heyliger, P. (2025b). On the accuracy of CEL blast simulations: validation and application. *Asian Journal of Civil Engineering*, *26*(2), 843–866. https://doi.org/10.1007/s42107-024-01226-2

Jablonski, J., Carlucci, P., Thyagarajan, R., Nandi, B., & Arata, J. (2012). *Simulating Underbelly Blast Events using Abaqus/Explicit -CEL*. 14.

Jayasinghe, L. B., Thambiratnam, D. P., Perera, N., & Jayasooriya, J. H. A. R. (2014). Blast response and failure analysis of pile foundations subjected to surface explosion. *Engineering Failure Analysis*, *39*, 41–54. https://doi.org/10.1016/j.engfailanal.2014.01.013

Keskin, İ., Yadgar Ahmed, M., Ramadhan Taher, N., Gör, M., & Zrar Abdulsamad, B. (2022). An evaluation on effects of surface explosion on underground tunnel; availability of ABAQUS Finite element method. *Tunnelling and Underground Space Technology*, *120*(September 2021). https://doi.org/10.1016/j.tust.2021.104306

King, K. W., & Vaught, C. R. (2008). Determining TNT Equivalency for Confined Detonations. *Volume 5: High Pressure*

*Technology; Nondestructive Evaluation Division; Student Paper Competition*, 89–100. https://doi.org/10.1115/PVP2008-61699

Kinney, G. F., Graham, K. J. (2013). *Explosive shocks in air*. Springer Science & Business Media.

Lee, E.L.; Hornig, H.C.; Kury, J. W. (1968). Adiabatic Expansion of High Explosive. In *Technical Report No. UCRL-50422*.

Liu, C., Zhao, G., He, J., Liu, H., & Cui, J. (2025). Damage Pattern and Failure Mechanism of Shield Tunnel Lining under Internal Explosion. *Thin-Walled Structures*, *214*, 113420. https://doi.org/10.1016/j.tws.2025.113420

Liu, L., Zong, Z., Gao, C., Yuan, S., & Lou, F. (2020). Experimental and numerical study of CFRP protective RC piers under contact explosion. *Composite Structures*, *234*. https://doi.org/10.1016/j.compstruct.2019.111658

Maier, W., Ramme, J., Dingler, M., & Möhring, H.-C. (2025). Coupled Eulerian-Lagrangian (CEL) simulation of the chip breaking in a single lip deep hole drilling process (SLD). *Procedia CIRP*, *133*, 72–77. https://doi.org/10.1016/j.procir.2025.02.014

Mobaraki, B., & Vaghefi, M. (2015). Numerical study of the depth and cross-sectional shape of tunnel under surface explosion. *Tunnelling and Underground Space Technology*, *47*, 114–122. https://doi.org/10.1016/j.tust.2015.01.003

Mougeotte, C., Carlucci, P., Recchia, S., & Ji, H. (n.d.). *2010 SIMULIA Customer Conference Novel Approach to Conducting Blast Load Analyses Using Abaqus/Explicit-CEL*. 1–15. http://www.simulia.com/download/scc-papers/Defense/novel-approach-conducting-blast-load-analyses-2010-F.pdf

Nagy, N. (2025). Nonlinear numerical modelling for the effects of surface explosions on buried reinforced concrete structures. *SSRN Electronic Journal*. https://doi.org/10.2139/ssrn.5267199

Nagy, N. M. (2015). Numerical evaluation of craters produced by explosions on the soil surface. *Acta Physica Polonica A*, *128*(2), 260–266. https://doi.org/10.12693/APhysPolA.128.B-260

*Orica-Nitro Explosives*. (2023). http://www.orica-nitro.com.tr/

*Oros-Or36-Datalogger*. (2023). https://www.oros.com/solutions/instruments-accessories/or36-mobipack-16-channels-teamwork-analyzer-recorder/

PW., C. (1996). *Explosives Engineering*. Wiley-VCH.

Qian, H., Zong, Z., Wu, C., Li, J., & Gan, L. (2021). Numerical study on the behavior of utility tunnel subjected to ground surface explosion. *Thin-Walled Structures*, *161*(June 2020), 107422. https://doi.org/10.1016/j.tws.2020.107422

Qiu, G., Henke, S., & Grabe, J. (2009). Applications of Coupled Eulerian-Lagrangian Method to Geotechnical Problems with Large Deformations. *SIMULIA Customer Conference*, *2001*, 1–16. http://www.simulia.com/download/pdf2009/Qiu_SCC2009.pdf

Rais, I., Asim Ansari, M., Sadique, M. R., Ansari, M. M., Alam, T., & Dobrotă, D. (2025). Finite element modelling and analysis of sustainable safety bunkers in war zones. *Sustainable and Resilient Infrastructure*, 1–24. https://doi.org/10.1080/23789689.2025.2496054

Sadek S., Dabaghi M., Elhajj I., Zimmaro P., Hashash Y. M. A., Yun S. H., O'Donnell T. M., & Stewart J. P. (2021). *Engineering impacts of the August 4, 2020 Port of Beirut, Lebanon explosion*.

Savaş, S., & Bakir, D. (2022). An experimental study on the blast responses of hollow core concrete slabs to contact explosions. *Revista de La Construcción*, *21*(3), 587–601. https://doi.org/10.7764/RDLC.21.3.587

Savaş, S., & Bakir, D. (2023). An investigation of the effects of the vehicle terror suicide attack in the urban area. *Engineering Failure Analysis*, *145*, 107049. https://doi.org/10.1016/j.engfailanal.2023.107049

Smith, P. D., & Hetherington, J. G. (1994). Blast and ballistic loading of structures. Butterworth-Heinemann, Oxford.

Sochet, I. (2010). Blast effects of external explosions. *Eighth International Symposium on Hazards, Prevention, and Mitigation of Industrial Explosions*.

Souli, M., & Shahrour, I. (2013). A coupling method for soil structure interaction problems. *International Journal for Numerical and Analytical Methods in Geomechanics*, *37*(9), 1140–1153. https://doi.org/10.1002/nag.2080

Stevens, D. J., & Krauthammer, T. (1991). Analysis of Blast-Loaded, Buried RC Arch Response. I: Numerical Approach. *Journal of Structural Engineering*, *117*(1), 197–212. https://doi.org/10.1061/(ASCE)0733-9445(1991)117:1(197)

van der Voort, M. M., van Wees, R. M. M., Brouwer, S. D., van der Jagt-Deutekom, M. J., & Verreault, J. (2015). Forensic analysis of explosions: Inverse calculation of the charge mass. *Forensic Science International*, *252*, 11–21. https://doi.org/10.1016/j.forsciint.2015.04.014

Veen, W. A. Van Der. (2003). *Simulation of a Compartmented Airbag Deployment Using an Explicit , Coupled Euler / Lagrange Method With Adaptive Euler Domains*.

Waga, J. M., & Fajer, M. (2021). The heritage of the Second World War: bombing in the forests and wetlands of the Koźle Basin. *Antiquity*, *95*(380), 417–434. https://doi.org/10.15184/aqy.2020.154

Wang, I.-T. (2019). Field Experiments and Numerical Analysis of the Ground Vibration Isolation of Shock Wave Propagation under Explosion Shock Loading. *Vibration*, *2*(4), 300–310. https://doi.org/10.3390/vibration2040019

Wang, I.-T. (2021). Numerical and Experimental Approach for Failure Analysis of Soil Subjected to Surface Explosion Loading. *Shock and Vibration*, *2021*(1). https://doi.org/10.1155/2021/4981507

Wang, J., Zhang, Y., Qin, Z., Song, S., & Lin, P. (2020). Analysis method of water inrush for tunnels with damaged water-resisting rock mass based on finite element method-smooth particle hydrodynamics coupling. *Computers and Geotechnics*, *126*(June), 103725. https://doi.org/10.1016/j.compgeo.2020.103725

Wang, M., Qiu, Y., & Yue, S. (2018). Similitude laws and modeling experiments of explosion cratering in multi-layered geotechnical media. *International Journal of Impact Engineering*, *117*, 32–47. https://doi.org/10.1016/j.ijimpeng.2017.11.018

Wang, W., Chen, Y., Liu, H., & Zhou, F. (2015). Experimental investigation of dynamic porewater pressure response induced by single shallow-buried detonations in saturated sand. *Géotechnique Letters*, *5*(3), 142–146. https://doi.org/10.1680/jgele.14.00083

Wang, Z., Hao, H., & Lu, Y. (2004). A three-phase soil model for simulating stress wave propagation due to blast loading. *International Journal for Numerical and Analytical Methods in Geomechanics*, *28*(1), 33–56. https://doi.org/10.1002/nag.325

Wang, Z., Lu, Y., Hao, H., & Chong, K. (2005). A full coupled numerical analysis approach for buried structures subjected to subsurface blast. *Computers & Structures*, *83*(4–5), 339–356. https://doi.org/10.1016/j.compstruc.2004.08.014

Wharton, R. ., Formby, S. ., & Merrifield, R. (2000). Airblast TNT equivalence for a range of commercial blasting explosives. *Journal of Hazardous Materials*, *79*(1–2), 31–39. https://doi.org/10.1016/S0304-3894(00)00168-0

Wu, J., Fan, Y., Leng, Z., & Yang, G. (2025). 2D Numerical Simulation of Blasting Crater and Breaking Fragmentations. *Computer Modeling in Engineering & Sciences*, *144*(1), 811–839. https://doi.org/10.32604/cmes.2025.065632

Xiang, X., & Zi-Hang, D. (2017). Numerical implementation of a modified Mohr–Coulomb model and its application in slope stability analysis. *Journal of Modern Transportation*, *25*(1), 40–51. https://doi.org/10.1007/s40534-017-0123-0

Xie, X., Yao, Y., Yang, G., & Jia, Y. (2017). Large-Scale Field Experiments on Blast-Induced Vibration and Crater in Sand Medium. *International Journal of Geomechanics*, *17*(8), 1–10. https://doi.org/10.1061/(asce)gm.1943-5622.0000877

Xu, R., Chen, L., Zheng, Y., Li, Z., Cao, M., & Fang, Q. (2021). Study of Crater in the Gobi Desert Induced by Ground Explosion of Large Amounts of TNT Explosive up to 10 Tons. *Shock and Vibration*, *2021*. https://doi.org/10.1155/2021/7357877

Yang, G., Wang, G., Lu, W., Zhao, X., Yan, P., & Chen, M. (2018). Numerical modeling of surface explosion effects on shallow-buried box culvert behavior during the water diversion. *Thin-Walled Structures*, *133*, 153–168. https://doi.org/10.1016/j.tws.2018.09.039

Yang, H., Kuang, K., Lu, Y., Ma, K., & Zhang, H. (2025). Research on the Application of the CEL Method to Reinforced Concrete Beams under a Close-Range Explosion Load. *Journal of Structural Engineering*, *151*(1). https://doi.org/10.1061/JSENDH.STENG-13486

Zhou, X. Q., Kuznetsov, V. A., Hao, H., & Waschl, J. (2008). Numerical prediction of concrete slab response to blast loading. *International Journal of Impact Engineering*, *35*(10), 1186–1200. https://doi.org/10.1016/j.ijimpeng.2008.01.004